A&A, 704, A221 (2025)
https://doi.org/10.1051/0004-6361/202556584

Astronomy & Astrophysics

WIde Separation Planets In Time (WISPIT)

Two directly imaged exoplanets around the Sun-like stellar binary WISPIT 1

Richelle F. van Capelleveen[1,⋆], Matthew A. Kenworthy[1], Christian Ginski[2], Eric E. Mamajek[3], Alexander J. Bohn[1], Rico Landman[1,4], Tomas Stolker[1], Yapeng Zhang[5], Nienke van der Marel[1], and Ignas Snellen[1]

[1] Leiden Observatory, Leiden University, Postbus 9513, 2300 RA Leiden, The Netherlands
[2] School of Natural Sciences, Center for Astronomy, University of Galway, Galway, H91 CF50, Ireland
[3] Jet Propulsion Laboratory, California Institute of Technology, 4800 Oak Grove Drive, M/S 321-162, Pasadena, CA, 91109, USA
[4] SRON Netherlands Institute for Space Research, Niels Bohrweg 4, 2333 CA Leiden, The Netherlands
[5] Department of Astronomy, California Institute of Technology, Pasadena, CA 91125, USA

Received 24 July 2025 / Accepted 25 August 2025

ABSTRACT

Context. Wide separation gas giant planets present a challenge to current planet formation theories, and the detection and characterisation of these systems enables us to constrain their formation pathways.
Aims. The WIde Separation Planets In Time (WISPIT) survey aims to detect and characterise wide separation planetary-mass companions over a range of ages from <5 to 20 Myr around solar-type host stars at distances of 75–500 (median 140) parsecs.
Methods. The WISPIT survey carries out two five-minute H-band exposures with the VLT/SPHERE instrument and IRDIS camera separated by at least six months to identify co-moving companions via proper motion analysis. These two H-band observations in combination with a follow-up K_s-band observation were used to determine the colour and magnitude of the co-moving companions and to derive their masses through comparison to AMES-COND and AMES-DUSTY evolutionary tracks.
Results. We report the discovery of WISPIT 1b and WISPIT 1c, two gas giant exoplanets that are co-moving with the stellar binary WISPIT 1, which itself consists of a K4 star and M5.5 star in a multi-decadal orbit. The planets are at projected separations of 338 au and 840 au and have masses of 10 M_J and 4 M_J, respectively.
Conclusions. We identified two common proper motion planetary companions of a (previously unknown) stellar binary with a Sun-like primary. These targets are ideal for follow-up characterisation with both ground- and space-based telescopes. Monitoring of the orbit with the GRAVITY interferometer will place constraints on their eccentricity, and spectroscopic characterisation will identify the composition and metallicity, providing information on their formation pathways.

Key words. planets and satellites: detection – planets and satellites: formation – stars: individual: WISPIT 1

1. Introduction

Gas giant planets are thought to form through either bottom-up or top-down formation mechanisms. In bottom-up formation, an embryonic rocky protocore first forms and subsequently accretes gas to become a gas giant via core accretion (CA; Pollack et al. 1996). While this is thought to be the dominant mode of planet formation, it becomes increasingly difficult for protocores to reach the critical mass required for gas accretion within the lifetime of the gas disk at separations much larger than the ice line (Mordasini et al. 2012). Somewhat larger separations for in situ formation of gas giants can be reached through pebble accretion (PA; Lambrechts & Johansen 2012). In contrast to classical CA, where the protocore grows by accreting planetesimals, with PA the protocore grows via accretion of small solid particles that are drifting radially inward. The efficiency of PA increases with stellar mass, and its relative efficiency compared to classical CA increases at larger separations, with the timescale to reach the critical core mass for gas accretion being shortened by a factor of 100 at 50 au (Lambrechts & Johansen 2012). Nonetheless, the semi-major axis preference reported for gas giant formation via PA is on the lower end of the 10–100 au range (Nielsen et al. 2019). Top-down formation mechanisms form a gas giant directly through gravitational collapse. This can either happen by turbulent fragmentation processes of the collapsing proto-stellar cloud (Kroupa 2001) or by gravitational instability (GI; Boss 1997), where the gas giant forms from the direct collapse of part of the circumstellar disk (see also the review by Kratter & Lodato 2016). Of top-down formation processes, the latter is thought to be the dominant planet formation mechanism, especially if the resulting planet is coplanar with the circumstellar disk and with other planets in the system. Whereas gas giants represent the high-mass outcome of bottom-up formation, they also represent the low-mass outcome of top-down formation (Nielsen et al. 2019), and while CA formation is more likely to occur at separations less than 35 au, GI formation is more likely to occur on wide orbits beyond 35 au (Dodson-Robinson et al. 2009).

To date, nearly a thousand of such gas giant planets with masses between 1 and 13 Jupiter masses have been detected and confirmed. Of these, fewer than 5%[1] have been discovered via direct imaging (DI), despite such planets being among the most

---

[⋆] Corresponding author: `capelleveen@strw.leidenuniv.nl`

[1] 41 out of 992 as of July 22, 2025, retrieved from the NASA Exoplanet Archive `https://exoplanetarchive.ipac.caltech.edu`

promising targets for atmospheric characterisation (e.g. Biller & Bonnefoy 2018). This low detection rate is primarily due to challenges inherent to direct imaging: gas giants are intrinsically faint, and their signal is typically overwhelmed by the flux from the host star, especially at small angular separations. Detecting them requires the use of starlight suppressing techniques and optics (e.g. Kenworthy & Haffert 2025), in combination with one or more post-processing techniques (e.g. Claudi & Mesa 2024; Follette 2023). Despite these challenges, several DI surveys conducted over the past two decades have successfully revealed self-luminous gas giant planets at separations of several hundreds of au down to a few au from their parent stars; these include the Gemini Deep Planet Survey (Lafrenière et al. 2007), GPIES (Macintosh et al. 2014; Nielsen et al. 2019), SPHERE SHINE (Chauvin et al. 2017; Vigan et al. 2021), SCExAO accelerating stars (Currie et al. 2025; El Morsy et al. 2024), and the BEAST survey (Delorme et al. 2024). Notable detections within 100 au of their host stars include the HR 8799 system (Marois et al. 2008, 2010), β Pic b (Lagrange et al. 2009) and c (Lagrange et al. 2020; Nowak et al. 2020), 51 Eri b (Macintosh et al. 2015), and more recently AF Lep b (Franson et al. 2023) and HD 135344 Ab (Stolker et al. 2025).

While direct imaging has revealed gas giant planets at a wide range of orbital separations, those detected at separations significantly larger than 100 au are particularly intriguing, as they present a challenge to planet formation theory. Among these detections are HD 106906 b (Bailey et al. 2014), YSES 1b (Bohn et al. 2019) and c (Bohn et al. 2020b), COCONUTS-2b (Zhang et al. 2021), and b Cen b (Janson et al. 2021). It is unclear whether such companions formed in situ through fragmentation or GI processes, or whether they formed closer to their host stars, either through top-down or bottom-up formation mechanisms, and were subsequently dynamically scattered to wide orbits. Disentangling these scenarios requires comparing observations with planet formation models, simulations, and predicted occurrence rates (Mordasini et al. 2009a,b; Forgan et al. 2018). Although tremendous effort and progress have been made, previous analyses have not yielded conclusive constraints on their formation pathways due to the small sample size of directly imaged wide separation gas giants (e.g. Vigan et al. 2017; Bowler & Nielsen 2018). One recent successful approach in expanding this sample size is the Young Suns Exoplanet Survey (YSES; Bohn et al. 2021, and van Capelleveen in prep.), a VLT/SPHERE survey of a homogeneous sample of 70 young solar-mass stars in the Lower Centaurus Crux (LCC) subgroup of the Scorpius-Centaurus association (~15 Myr, ~120 pc; Pecaut & Mamajek 2016). Among its findings is YSES 1 (Bohn et al. 2020a; Bohn et al. 2020b), the first multi-planet system around a young solar analogue.

The WIde Separation Planets In Time (WISPIT) survey extends the scope of YSES by targeting young Sun-like stars spanning a broader range of ages and other regions of the sky. To investigate whether wide orbit gas giants form in situ or form closer to their host star and are subsequently scattered outward, it is necessary to sample stars from the earliest timescales of top-down formation (0.5 Myr) to the end of bottom-up formation (5–10 Myr). This age-diverse sample of young solar-type stars was constructed from the pre-main sequence catalogue of stars younger than 20 Myr compiled by Zari et al. (2018). This sample is magnitude limited (G<13 mag) to enable AO-assisted imaging with VLT/SPHERE. After applying selection criteria based on youth indicators, stellar mass, suitability for common proper motion analysis, and observability with VLT/SPHERE, we obtained a final sample of 178 solar-mass stars with ages ranging from <5 to 20 Myr (median: 8.5 Myr) and distances from 75 to 500 pc (median: 140 pc).

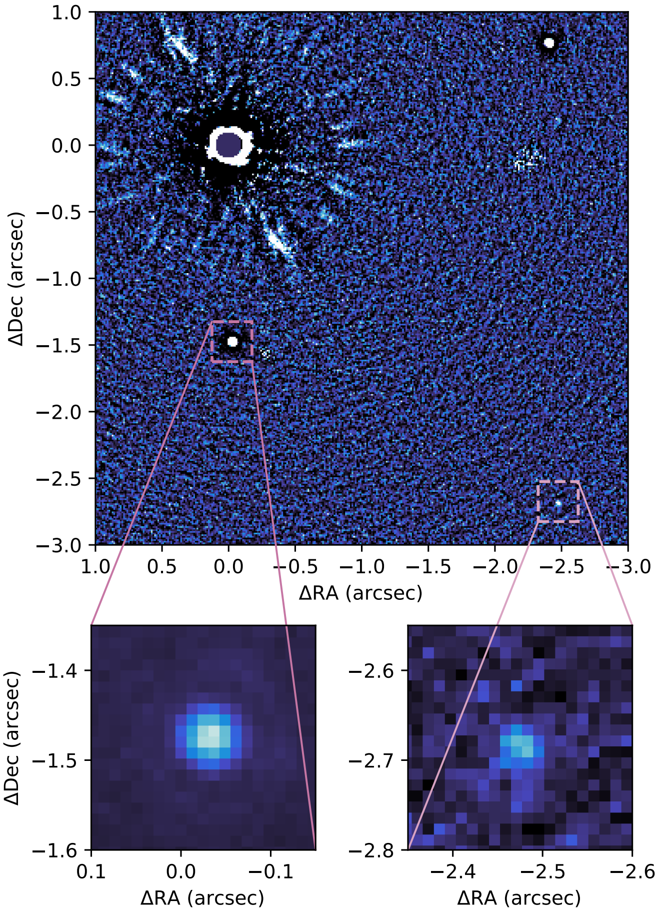

Fig. 1. Detail of the WISPIT 1 system. The top panel shows the SPHERE/IRDIS H-band image taken on 2022 November 19, processed with unsharp masking to suppress the stellar halo. The stellar binary WISPIT 1 (behind the coronagraph) is located in the upper left, with its companions highlighted with coloured boxes. Zoomed-in images of the unmasked observation centred on companions WISPIT 1b and WISPIT 1c, are shown in the lower left and lower right panels, respectively.

In this paper, we present the first discovery of this survey: WISPIT 1. This young (~16 Myr) system located 229 parsecs away is a stellar binary with a solar-type primary, and it hosts two co-moving planetary mass companions at large semimajor axes (see Fig. 1). After introducing our proposed nomenclature for the survey, we describe the observations (Sect. 3) and the data reduction (Sect. 4). We present an analysis of the WISPIT 1 stellar components and the companions of the system in Sect. 5. In Sect. 6, we discuss the results and place them in the broader context of known systems. Finally, we summarise our findings and outline recommendations for future observations in Sect. 7.

2. Nomenclature of the WISPIT targets

The WISPIT survey will have a dedicated catalogue that will be used for all targets in the survey. The WISPIT acronym has been accepted by the IAU Commission B2 Working Group on Designations and has subsequently been registered in the dictionary[2] of the Simbad database (Wenger et al. 2000). The nomenclature

---

[2] `https://cds.unistra.fr/cgi-bin/Dic-Simbad`

for the WISPIT acronym follows a 2x2 format, with two characters representing the star and two representing the planet. Here the host star is identified as WISPIT NNN, where *NNN* is an ordinal number with at most three digits. WISPIT NNNb is its planet, where *b* is generic and may also be *c, d,* etcetera. WISPIT NNNA is the host star that is itself a component of a common proper motion system (CPMS), where *A* may also extend to *B, C,* and so on. We note that in a CPMS with components *A* and *B*, by definition *A* designates the brighter star of the system. If the stars in a CPMS are well separated or if the secondary component is significantly fainter than the primary, using *NNNA* and *NNNAb* is not necessary. Instead, *NNN* and *NNNb* can be used for the primary star and its planet, respectively, with *NNNB* assigned to a wide and/or faint stellar companion. As the survey contains 178 targets, the highest ordinal number assigned is 178; the final target in the survey will thus be named WISPIT 178. For instance, if this target were to be a stellar binary with a planet orbiting the secondary star, the primary would be named WISPIT 178A with secondary WISPIT 178B that has a planet WISPIT 178Bb.

Following the nomenclature described above, the first target in the survey is designated as WISPIT 1, with its planets WISPIT 1b and WISPIT 1c. Here WISPIT 1 refers to the primary star in the binary system, and WISPIT 1B denotes the significantly fainter secondary star.

3. Observations

The combined stellar properties of WISPIT 1 are listed in Table 1. WISPIT 1 has been observed on UTC 2022-11-19T08, UTC 2023-12-03T08, and UTC 2024-11-30T06 as part of the WISPIT survey in programs 110.23XJ.003, 112.25X3.003 and 114.27EK.003 respectively. Observations were taken with Spectro-Polarimetric High-contrast Exoplanet REsearch (SPHERE; Beuzit et al. 2019), the coronagraphic facility mounted at the Nasmyth platform of 8.2m Unit Telescope 3 (UT3) of the Very Large Telescope (VLT). To correct for atmospheric turbulence and internal defects, SPHERE utilises the extreme adaptive optics (AO) module called SPHERE AO for eXoplanet Observation (SAXO; Fusco et al. 2006, 2014). All observations were conducted in Classical Imaging (CI) mode using the Infrared Dual-band Imager and Spectrograph (IRDIS; Dohlen et al. 2008) in pupil-stabilised mode. The first two epochs use broadband filter H and the third epoch uses broadband filter K_s. To avoid saturation by the primary star in the science exposures, an apodized Lyot coronagraph was used to attenuate the stellar halo (Soummer 2005; Carbillet et al. 2011). An overview of the setup and observation conditions of the science observations is provided in Table 2. In addition to these science frames, we obtained center frames, sky frames and flux frames. The center frames are acquired by applying a sinusoidal pattern to the deformable mirror, creating a waffle pattern to determine the star's position behind the coronagraph. The sky frames are taken at an offset position without AO correction and without any sources in the field of view, enabling the subtraction of instrumental and thermal background. The flux frames serve as a photometric reference for detected point sources in the science frames, and are taken without a coronagraph. In H-band, near-infrared neutral density filter ND1.0[3] was used to allow for longer exposures without saturating the detector.

Table 1. IDs, astrometry and photometry for WISPIT 1.

Parameter	Value	Ref.
Gaia DR3	5517037434775143808	(1)
2MASS	J07511168-5008158	(2)
WISE	J075111.66-500815.8	(3)
TIC	268764100	(4)
RA* α [deg]	117.79855076351	(1)
Dec* δ [deg]	-50.13768323600	(1)
Parallax ϖ [mas]	4.3652 ± 0.0137	(1)
Distance d [pc]	$228.85^{+0.59}_{-0.68}$	(5)
Pmra μ_α [mas/yr]	-19.824 ± 0.016	(1)
Pmdec μ_δ [mas/yr]	14.021 ± 0.017	(1)
v_r [km/s]	21.08 ± 5.61	(1)
v_r [km/s]	19.9 ± 3.0	(6)
v_r [km/s]	19.0 ± 3.0	(6)
G [mag]	12.722928 ± 0.002907	(1)
$B_p - R_p$	1.427105	(1)
$B_p - G$	0.642953	(1)
$G - R_p$	0.784152	(1)
B [mag]	14.171 ± 0.052	(7)
V [mag]	13.146 ± 0.044	(7)
$B - V$ [mag]	1.026 ± 0.068	(7)
g' [mag]	13.655 ± 0.022	(7)
r' [mag]	12.725 ± 0.029	(7)
i' [mag]	12.297 ± 0.009	(7)
J [mag]	10.859 ± 0.026	(2)
H [mag]	10.301 ± 0.023	(2)
K_s [mag]	10.121 ± 0.019	(2)
$W1$ [mag]	10.040 ± 0.023	(8)
$W2$ [mag]	10.016 ± 0.020	(8)
$W3$ [mag]	9.908 ± 0.042	(8)

Notes. *=ICRS, epoch J2016.0 References: (1) Gaia Collaboration (2021), (2) Cutri et al. (2003), (3) Cutri & et al. (2012), (4) Stassun et al. (2019), (5) Bailer-Jones et al. (2021), (6) Žerjal et al. (2021), (7) Henden et al. (2016), (8) Cutri et al. (2013).

4. Data reduction

All SPHERE observations have been (pre-)processed with (modified) PynPoint modules (Amara & Quanz 2012; Stolker et al. 2019). This includes bad pixel removal, flatfielding, sky subtraction, anamorphic distortion correction, centring, derotating and median combining the exposures. The anamorphic distortion (see Maire et al. 2016) is corrected by multiplying the y-axis by 1.0062 ± 0.0002, as stated in the SPHERE manual[4]. The images are derotated to the parallactic angle on the sky and the static pupil offset of 135.99 ± 0.11 deg. An additional rotation of 1.76 ± 0.04 deg was applied to correct for the true north offset (Maire et al. 2021). The pixel scales used for astrometric calibration are 12.246 ± 0.009 mas yr^{-1} in H-band and 12.266 ± 0.009 mas yr^{-1} in K_s-band based on the five-year analysis of SPHERE astrometric calibration data presented in Maire et al. (2021).

Inspection of flux frames showed that an unknown observational issue caused all first flux frames of all three observations to be unusable due to lower signal and duplicated sources on the

---

[3] For filter description and transmission (see `https://www.eso.org/sci/facilities/paranal/instruments/sphere/inst/filters.html`).

[4] SPHERE manuals: `https://www.eso.org/sci/facilities/paranal/instruments/sphere/doc.html`

Table 2. SPHERE/IRDIS observations of WISPIT 1.

Observation date (yyyy-mm-dd)	Filter	Coronagraph	NEXP×NDIT×DIT (1×1×s)	ω ($''$)	X	τ_0 (ms)
2022-11-19	H	N_ALC_YJH_S	4×2×32	0.565 ± 0.009	1.116 ± 0.001	3.800 ± 0.346
2023-12-03	H	N_ALC_YJH_S	4×2×32	0.290 ± 0.000	1.110 ± 0.000	13.900 ± 0.000
2024-11-30	K_s	N_ALC_Ks	7×1×64	0.481 ± 0.010	1.151 ± 0.003	6.700 ± 0.545

Notes. Observation setup and conditions for all WISPIT 1 observations. All filters are SPHERE broadband filters. The total integration time is the product of the number of exposures (NEXP), the number of sub-integrations per exposure (NDIT) and the detector integration time (DIT). The seeing is denoted by ω, the airmass by X and the coherence time by τ_0.

detector. It appears to be specific to an attribute of the observation of this source, as it is not present in most observations of other WISPIT targets with the same observation setup. To address this issue, in both H-band observations the first seven flux frames were discarded and in the K_s-band observation the first three flux frames were discarded.

The median-combined unsharp-masked image of the 2022 H-band exposures, highlighting the planetary-mass companions, is shown in Fig. 1. Annotated images of the median-combined observations from all epochs, along with a discussion of their noise properties, are included in Appendix A.

5. Results and analysis

WISPIT 1 is a close stellar binary; we discuss its properties in Sect. 5.1 and show that it exhibits negligible relative motion over our two-year baseline. The photometry and age of the primary are derived in Sect. 5.2. In Sect. 5.3, we demonstrate that WISPIT 1b and WISPIT 1c share common proper motion with the star, and in Sect. 5.4 we show that their photometry is consistent with planetary mass objects.

5.1. WISPIT 1 is a stellar multiple

SPHERE flux calibration images of WISPIT 1 revealed it to be a previously unresolved binary (see Fig. 2). All three epochs show the presence of a marginally spatially resolved secondary companion to the north-west of the primary star. To confirm that the secondary star is bound and shows minimal orbital motion over a period of two years, as well as to disentangle the flux of the primary star from that of the secondary star, we used a Markov chain Monte Carlo (MCMC; MacKay 2003) fitting routine to determine their relative positions and flux ratio. We constructed synthetic model binary stars from normalised median PSFs and used MCMC to obtain the best-fit model. To estimate the median PSF in H and K_s bands, we leveraged flux observations of single stars from YSES to construct normalised median PSFs, with peak flux scaled to unity. The sources used to create these PSFs are listed in Appendix G. These median PSFs were then rotated according to the position angles of the flux frames of the WISPIT 1 observations. To model the binary in the imaging data, we defined a log-probability function composed of a log-likelihood and log-prior term, evaluated using the `emcee` MCMC sampler (Foreman-Mackey et al. 2013). The free parameters θ describe the offsets in x and y with respect to the centre of the frame and the peak fluxes of the primary and the secondary star. The log-likelihood was computed as

$$\ln \mathcal{L}(\theta) = -\frac{1}{2} \sum_i \left(\frac{D_i - M_i(\theta)}{\sigma_i} \right)^2 ,$$

where D_i and $M_i(\theta)$ are the observed and model pixel values respectively, σ_i is the corresponding uncertainty, and the sum is performed over pixels selected in a mask around both stars. We assume Gaussian noise with a standard deviation of 5% of the signal. The synthetic model image $M(\theta)$ is generated by placing the median PSFs at the positions and with peak fluxes specified by θ. The log-prior constrains the stellar flux to be positive; it returns $\ln P(\theta) = 0$ when all fluxes are strictly positive, and $-\infty$ otherwise. The total log-probability is then given by

$$\ln \mathcal{P}(\theta) = \ln P(\theta) + \ln \mathcal{L}(\theta),$$

which is used to evaluate the posterior probability during sampling. We used 128 walkers and 30 000 iterations, discarded the first 1500 steps and thinned every 250 steps. All free parameters converged to Gaussian distributions; the resulting parameters are listed in Table 3. The fitting routine underestimates the positional errors, so instead we adopted errors in offset of 2.5 mas (~0.2 pixel), corresponding to the SPHERE centring precision. The error in the peak flux is derived from the root mean square (rms) of the residuals. Fig. 2 shows the observed image, the best-fit synthetic model image and the residuals for all three epochs.

The astrometric fits show negligible relative motion of the secondary to the primary star, inconsistent with the proper motion of a distant background source. The interpretation of WISPIT 1 as a binary system is consistent with the *Gaia* DR3 renormalised unit weight error (RUWE) of 1.488, which also suggests that the source may be non-single. The measured positions of WISPIT 1 correspond to a binary with a physical projected separation of at least 10.5 au, which, assuming a circular Keplerian orbit, corresponds to a period of at least 34 years. We conclude that this is a gravitationally bound secondary companion, and that its presence has a negligible effect on the observed motion of other sources in the field over a baseline of two years.

5.2. Photometric analysis and age classification of the primary star

The peak fluxes from the binary fit cannot be directly converted to stellar magnitudes. Moreover, we note that the H-band and K-band fluxes listed in Table 3 are not directly comparable due to attenuation in the H-band by an ND-filter. Instead, we used the flux ratio in combination with the 2MASS magnitudes (see Table 1) of the unresolved system to derive individual magnitudes for the primary and secondary stars. Since the observed total flux in the H-band was higher in 2023 than in 2022, we used the weighted mean of the stellar fluxes across epochs to compute the H-band flux-ratio. The derivation of the individual apparent magnitudes is included in Appendix D. The resulting $H - K_s$

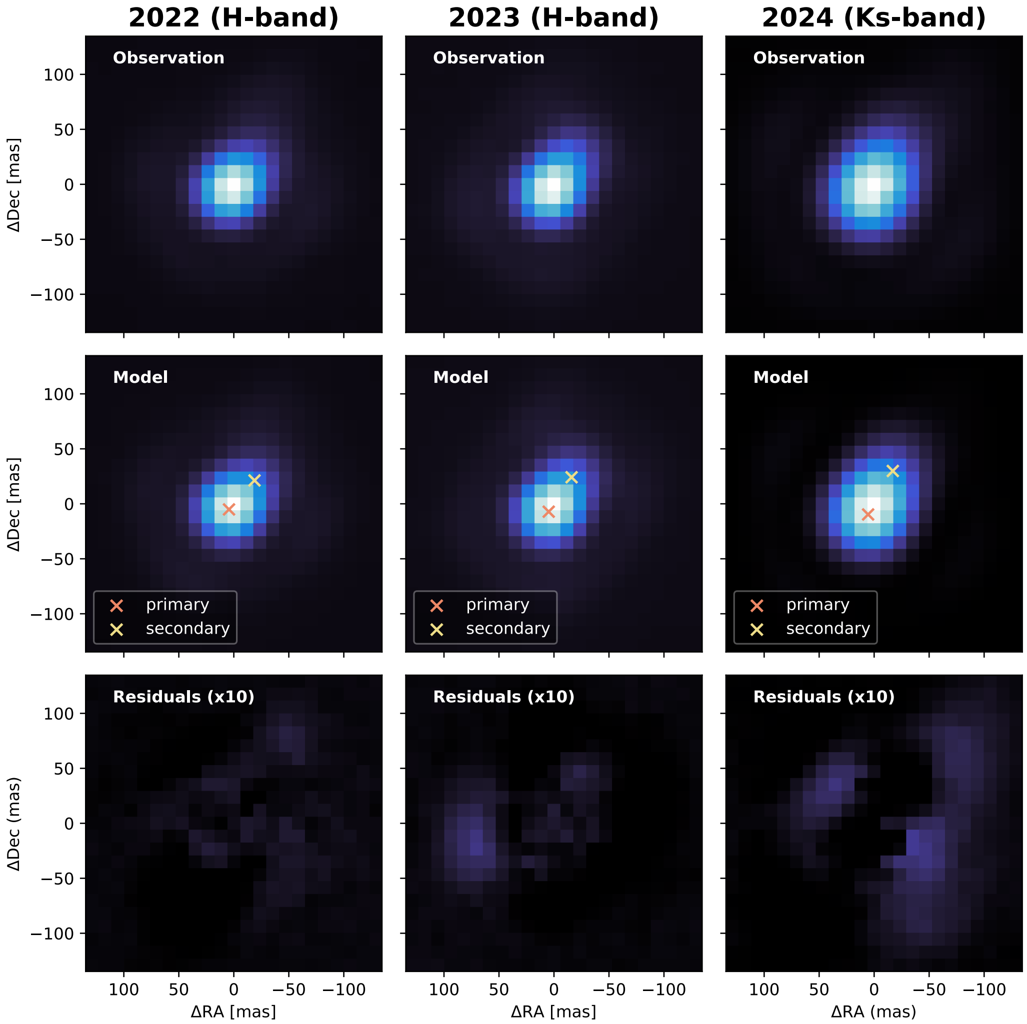

Fig. 2. Synthetic binary model fit to the flux calibration images of WISPIT 1 over three different epochs. The top row shows the observation; the second row shows the best-fit synthetic binary model, with the best-fit positions of the primary star and secondary star marked with crosses; the bottom row shows the residuals. The model and residuals inherit the colour scale from the corresponding observation, demonstrating the similarity in intensity between model and observation. The residual images are multiplied by a factor of ten, and show minor structures on the order of magnitude of less than ~5% of the peak flux of the observation.

Table 3. Best-fit parameters of a synthetic binary model to WISPIT 1.

		Primary			Secondary		
Observation date (yyyy-mm-dd)	Filter	Peak flux (ADU)	Δx (pixels)	Δy (pixels)	Peak flux (ADU)	Δx (pixels)	Δy (pixels)
2022-11-19	H	2998 ± 23	−0.357 ± 0.204	−0.418 ± 0.204	988 ± 23	1.536 ± 0.204	1.736 ± 0.204
2023-12-03	H	2908 ± 28	−0.391 ± 0.204	−0.585 ± 0.204	1170 ± 28	1.307 ± 0.204	1.972 ± 0.204
2024-11-30	K_s	7109 ± 80	−0.447 ± 0.204	−0.791 ± 0.204	3095 ± 80	1.387 ± 0.204	2.439 ± 0.204

colour was used to estimate the effective temperature and spectral type based on Table 5 of Pecaut & Mamajek (2013)[5]. The derived apparent magnitudes, colour, effective temperature and estimated spectral type are presented in Table 4.

We performed a χ^2 fit of a total of 19 photometric points from 2MASS (Cutri et al. 2003), WISE (Cutri & et al. 2012), DENIS (Epchtein et al. 1999), NEOWISE (Mainzer et al. 2014), APASS DR9 (Henden et al. 2016), and Gaia DR3 (Gaia Collaboration 2021) to synthetic models from BT-Settl CIFIST (Allard et al. 2013) with Virtual Observatory SED Analyzer (VOSA; Bayo et al. 2008). We constrained the extinction to $A_v = 0.047$ as derived in Appendix C. The temperatures were constrained based on the derived ranges presented in Table 4. The fit parameters of the primary were constrained to be in ranges $4300 \leq T_{\text{eff}} \leq 5300$ and $4 \leq \log g \leq 5$, and the fit parameters of the secondary were constrained to be in ranges $2600 \leq T_{\text{eff}} \leq 3400$ and $4 \leq \log g \leq 5.5$. The best-fit consistent with the observed flux ratios in H- and K_s-band is presented in Fig. 3.

---

[5] Spectral table from `https://www.pas.rochester.edu/~emamajek/EEM_dwarf_UBVIJHK_colors_Teff.txt` version 2022-04-16.

Table 4. Colour and apparent magnitudes of WISPIT 1A and WISPIT 1B.

Star	H (mag)	K_s (mag)	$H - K_s$ (mag)	T (K)	Spectral type
Primary (A)	10.63 ± 0.04	10.51 ± 0.02	0.12 ± 0.04	4670^{+990}_{-540}	K4V (G5V–K7V)
Secondary (B)	11.75 ± 0.08	11.42 ± 0.03	0.34 ± 0.09	2900^{+560}_{-280}	M5.5V (M2.5V–M7.5V)

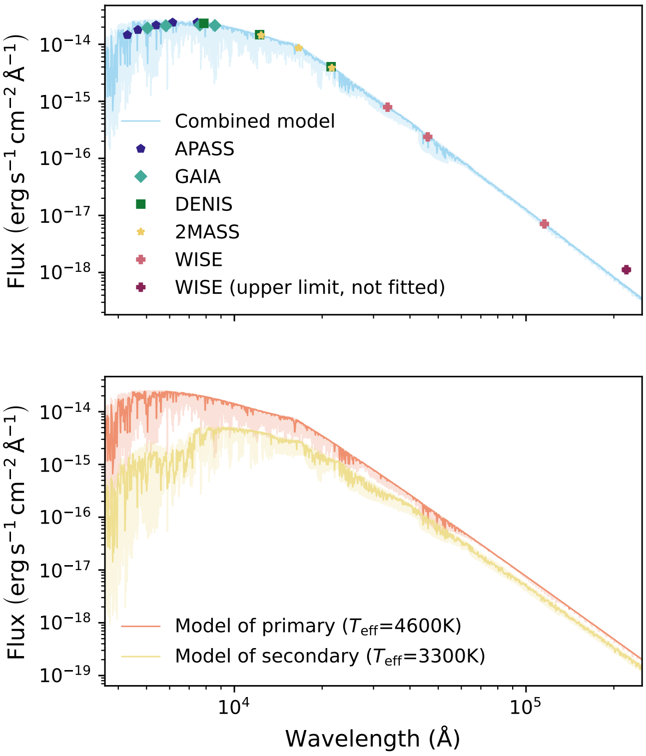

Fig. 3. Spectral energy distribution (SED) of WISPIT 1 with the best-fit BT-Settle-CIFIST binary model ($\chi_r^2 = 5.1$). Spectra are presented as a low resolution (high opacity) version overlaid on the high resolution (low opacity) version. The top panel displays photometric data from various sources, represented by coloured markers, alongside the combined model spectrum of the primary and secondary components. The bottom panel presents the individual model spectra for the primary and secondary star. Best-fit parameters for the primary are $T_{\rm eff} = 4600\,$K, $\log g = 4.0\,$dex, and $L_{\rm bol} = 0.36\,L_\odot$. Best-fit parameters for the secondary are $T_{\rm eff} = 3300\,$K, $\log g = 4.5\,$dex, and $L_{\rm bol} = 0.09\,L_\odot$.

Žerjal et al. (2021) report two equivalent width measurements of lithium absorption lines of WISPIT 1 measured with the Wide Field Spectrograph (WiFeS; Dopita et al. 2007). We computed the weighted mean using the inverse variance derived from the S/N ratio of each measurement, resulting in an equivalent width of EW(Li)=0.325 ± 0.009 Å. We adapted the isochrones from Žerjal et al. (2021) to $H - K_s$ colour using Table 5 from Pecaut & Mamajek (2013); these are presented in Fig. E.1 in Appendix E. As supported by the SED fit presented in Fig. 3, the flux at the Li I 6708 Å line is dominated by the primary star; the secondary star is not expected to contribute to the lithium absorption measurement. Therefore, in our calculations of the age of WISPIT 1, we assume that the equivalent width measurement is solely due to the primary star. The age is sampled by interpolating samples from the H, K_s, and EW(Li) distributions to the model isochrone grid presented in Fig. E.1. The resulting sampled age is $15.6^{+1.4}_{-1.2}$ Myr, consistent within uncertainties with the reported age of $16.8^{+3.5}_{-3.9}$ Myr (Kerr et al. 2021) for co-moving co-distant star 2MASS J07485619-4656229 (see Appendix B). However, these errors are inferred only from the uncertainty on the EW(Li) measurement itself and the uncertainty on the photometry. In reality, the cosmic scatter in lithium abundances would dominate the error on the age, so the formal errors on the age are likely underestimated. To provide a more conservative estimate, and to bring the uncertainties in line with those typically reported in literature for age determinations (including that of the co-moving companion), we inflate the age uncertainties by a factor of three and adopt an age of $15.6^{+4.1}_{-3.7}$ Myr.

5.3. Astrometric analysis

WISPIT 1b and WISPIT 1c are confirmed bound companions to WISPIT 1 based on common proper motion. Fig. 1 indicates the positions of both planets, which shows that they both lie beyond the extent of the stellar point spread function (PSF) halo. This enabled astrometric measurements to be obtained by fitting a 2D Gaussian to the approximate positions of the companions in the median combined science frames. The fitting method used to fit the `Astropy` (Astropy Collaboration 2013, 2018, 2022) 2D Gaussian model to the estimated positions was the `TRFLSQFitter`, a Trust Region Reflective algorithm with bound constraints and least-squares statistics. The fitting was constrained such that the centre of the Gaussian must lie within 5 pixels in both x and y direction of the manually estimated companion position. As an additional constraint, the Gaussian standard deviation was limited to be within 2.0 pixels of the median PSF standard deviation in the corresponding photometric band to ensure that the fitted full width at half maximum (FWHM) is consistent with that of SPHERE observations. The median PSF used to determine these constraints is constructed from observations from the Young Suns Exoplanet Survey (YSES; Bohn et al. 2020a, and van Capelleveen, in prep.), and is described in detail in Appendix G.

The uncertainties in pixel positions are taken from the covariance matrix of the Gaussian fit. In conversion of pixel positions to separation (arcseconds) and position angle (degrees), uncertainties in pixel scale, true north correction, and pupil offset – as detailed in Sect. 4 – are taken into account. Additionally, the centring precision of 2.5 mas of positioning the star behind the coronagraph is included in the error budget. The resulting positions for WISPIT 1b and WISPIT 1c are listed in Table 5. Using the *Gaia* DR3 distance to WISPIT 1 (see Table 1) this places WISPIT 1b and WISPIT 1c at projected physical separations of 338 and 840 au respectively. We present the measured positions of the companions alongside predicted background tracks for stationary background objects in Fig. 4, and used `backtracks`[6] (Balmer et al. 2025) to calculate the χ^2 between the measured

---

[6] `https://github.com/wbalmer/backtracks`

Table 5. Astrometry of WISPIT 1b and WISPIT 1c.

		1b		1c	
Observation date (yyyy-mm-dd)	Filter	Separation (″)	Position angle (°)	Separation (″)	Position angle (°)
2022-11-19	H	1.476 ± 0.006	181.27 ± 0.24	3.658 ± 0.023	222.54 ± 0.36
2023-12-03	H	1.474 ± 0.003	181.04 ± 0.13	3.662 ± 0.019	222.58 ± 0.29
2024-11-30	K_s	1.484 ± 0.007	181.13 ± 0.28	3.667 ± 0.038	222.49 ± 0.61

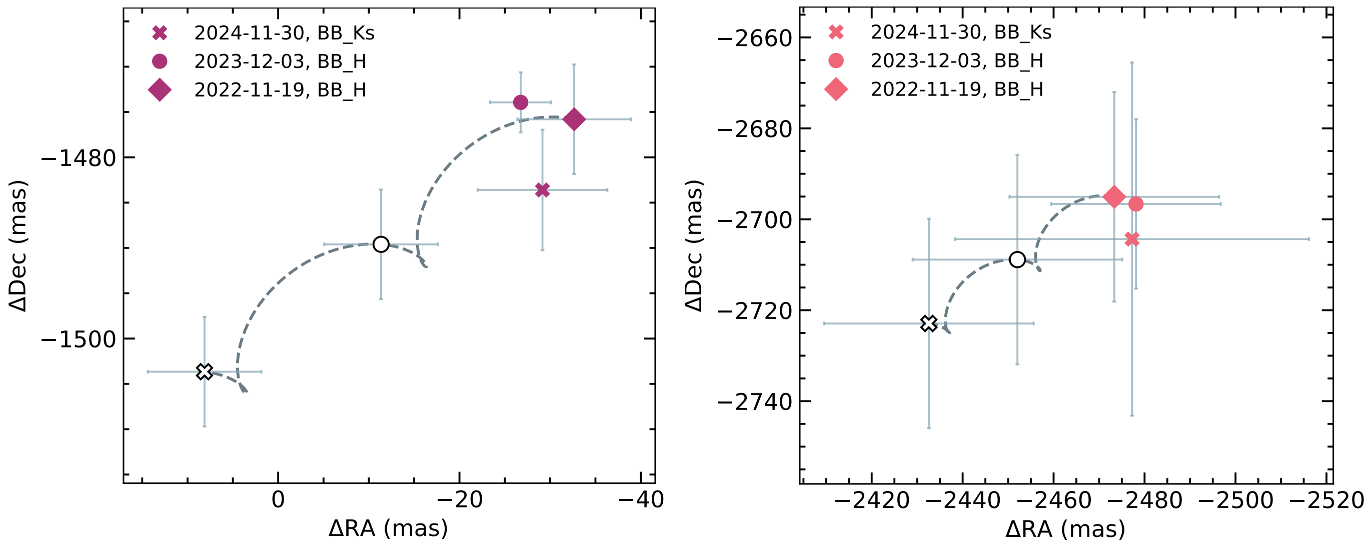

(a) WISPIT 1b

(b) WISPIT 1c

Fig. 4. Proper motion analysis of WISPIT 1b and WISPIT 1c. Each epoch is marked with a unique marker shape: diamond (2022), circle (2023), and cross (2024). The coloured version of the marker indicates the measured position of the companion. The unfilled (black outline, white centre) version of this marker indicates the position that the companion would have been at at the corresponding date if it were a background object. The dashed curve depicts the parallactic track of a background object from first epoch to last epoch. The χ^2 between the measured positions and the background track is 78.2 for WISPIT 1b and 3.8 for WISPIT 1c.

positions and the stationary background tracks. WISPIT 1b has a χ^2 of 78.2, reflecting the visual disagreement with the stationary background track. WISPIT 1c has a relatively small χ^2 of 3.8. This low value is primarily driven by the large astrometric uncertainties, as the clustering of the astrometric measurements around the first epoch position is visually similar to that of WISPIT 1b. For comparison, the background sources in the field of view (see Fig. F.1) show better agreement with the stationary background tracks, yielding χ^2 values of 10.6, 1.1 and 32.2. The latter higher value is attributable to a discrepancy in the position of the third epoch, which we suspect may be caused by binarity. Unlike these background sources, which visually follow the predicted background tracks, both 1b and 1c show minimal motion with respect to the star. Given their large projected physical separations from the host, this negligible observed motion over a two-year baseline is consistent with their interpretation as wide-orbit bound companions.

5.4. Photometric analysis

To assess whether the photometry of the bound companions is consistent with that of planetary-mass objects, we extracted photometry in two broadband filters, H and K_s, and fitted isochrones to estimate their mass. Considering the large angular separation between the companions and the star, both companions are in the background-limited regime of the observations, which allowed for using background-subtracted aperture photometry for flux extraction.

To derive the magnitudes of the companion candidates, we utilised the 2MASS magnitudes of the host star listed in Table 1. The binary is not resolved by 2MASS; their reported magnitudes correspond to the combined flux of the primary and the secondary star. To ensure consistency when computing the magnitude contrast, we used an aperture that is large enough to encompass the majority of the flux from both the primary and the secondary star. Specifically, we adopted an aperture with a radius of twice the FWHM of the median PSF in that photometric band (see Appendix G), resulting in radii listed in Table 6. The flux frames were already centred on the binary by the PynPoint reduction routine, but more precise centring for aperture photometry was done by fitting a 2D Gaussian with the same fitting routine as described in Sect. 5.3. The centre was constrained to lie within 5 pixels of the centre of the frame and the standard deviations of the fit were bounded to ±1.5 times the standard deviation of the median PSF. These constraints were not actively limiting in any frame, and served primarily as a safeguard. The final stellar flux was computed as the median of the flux from the individual frames, with uncertainties given by the standard deviation of the flux from these frames scaled by the ratio of the FWHM standard deviation to the FWHM mean across the frames. In both photometric bands, the stellar flux was scaled to the science frames by applying a scale factor that accounts for

Table 6. Photometric statistics and flux contrast of WISPIT 1b and WISPIT 1c.

			1b			1c		
Observation date (yyyy-mm-dd)	Filter	Ap. rad. (pix)	S/N	FPF	Flux contrast	S/N	FPF	Flux contrast
2022-11-19	H	8.47	27.0	9.9×10^{-27}	$(3.8 \pm 0.7) \times 10^{-4}$	5.6	1.3×10^{-7}	$(2.3 \pm 0.5) \times 10^{-5}$
2023-12-03	H	8.47	66.8	2.3×10^{-35}	$(3.7 \pm 0.7) \times 10^{-4}$	4.8	3.3×10^{-6}	$(1.3 \pm 0.4) \times 10^{-5}$
2024-11-30	K_s	10.27	53.8	2.7×10^{-24}	$(8.6 \pm 0.4) \times 10^{-4}$	1.7	4.3×10^{-2}	$(7.1 \pm 1.2) \times 10^{-5}$

Notes. Photometric detection statistics for both companions. The aperture radius (Ap. rad.) is the radius used to extract the photometry of the sources. The confidence of the detection is denoted by the S/N ratio as described by Mawet et al. (2014) and FPF denotes the false positive fraction. The flux contrast with WISPIT 1 is corrected for neutral density filters where relevant.

Table 7. Apparent and absolute magnitudes and colours of WISPIT 1b and WISPIT 1c.

Component	m_H (mag)	M_H (mag)	m_{K_s} (mag)	M_{K_s} (mag)	$H - K_s$ (mag)
WISPIT 1b	$18.87^{+0.35}_{-0.27}$	$12.07^{+0.35}_{-0.27}$	$17.78^{+0.05}_{-0.05}$	$10.98^{+0.05}_{-0.05}$	$1.09^{+0.31}_{-0.23}$
WISPIT 1c	$22.16^{+0.46}_{-0.32}$	$15.37^{+0.46}_{-0.32}$	$20.49^{+0.20}_{-0.17}$	$13.69^{+0.20}_{-0.17}$	$1.69^{+0.31}_{-0.24}$

the exposure time difference. In H-band, the measured stellar flux was also attenuated due to use of an ND filter. To account for this we scaled the extracted flux to the science frames by using a factor that combined the exposure time ratio and the ND filter transmission. Here the ND filter transmission was calculated as the weighted average of the ND filter's transmission across the broadband filter profile. The total scaled stellar flux and uncertainties are presented in Table 3.

The flux from the companions in the field was extracted by using an aperture of the same radius as used for the stellar aperture (see Table 6), centred on the companion position determined in astrometric analysis (Sect. 5.3). For noise estimation, we used a modified version of the PynPoint module `falsealarm`, which estimates background flux by selecting background apertures of equal radius located at the same separation from the star. The two apertures closest to the companions were excluded to avoid contamination. To mitigate the influence of bad pixels and/or field sources in the noise apertures, as an adjustment to the module we applied `astropy.stats` sigma-clipping with a 2σ threshold and five iterations to the background apertures. The noise statistics are given by the standard deviation of the integrated flux in the noise apertures multiplied with a correction factor to account for small sample statistics, following the methods from Mawet et al. (2014, Eq. (8)). For each companion, the signal, S/N ratio, false positive fraction and flux contrast with the binary were computed as weighted means from individual frame measurements. These results are summarised in Table 6 and were used in further analysis.

The flux contrast with the binary was converted to magnitude contrast. The apparent magnitude was then derived by assuming that the total measured stellar flux corresponds to the 2MASS catalogue value for the host star. Absolute magnitudes for the companions were calculated by using the Gaia DR3 derived distance to the system (Table 1). Apparent and absolute magnitudes of the companions are listed in Table 7. We note a slight discrepancy in the H-band magnitude between the 2022 and 2023 epochs for both companions, as well as all other field sources, with a lower magnitude (i.e., brighter) measured in 2023. This can be attributed to a higher measured stellar flux in 2023, resulting in a lower flux contrast of all candidate companions. Additionally, we note that the signal and S/N are lower in K_s-band than in H-band, especially for WISPIT 1c. This is due to a higher background noise overall, as well as a thermal background pattern typical of SPHERE K_s-band observations, which is especially prominent near the position of 1c on the detector (see Fig. A.3 in Appendix A). The colour-magnitude of the companions, along with 15.6 Myr AMES-COND and AMES-DUSTY isochrones (Allard et al. 2001; Chabrier et al. 2000) and other confirmed planets with available magnitudes in both H and K_s-bands, is shown in Fig. 5. WISPIT 1c is among the faintest exoplanets discovered in these bands, which is especially astonishing considering the confirmation required only two short exposures. However, we note its similarity to YSES 1c (Bohn et al. 2020b), of which no K_s measurement exists.

The masses of the companions are estimated by interpolating to AMES models retrieved in colour-magnitude space with `species` (Stolker et al. 2020). We sampled from the companions' respective asymmetric H-magnitude, K_s-magnitude and age distributions, and interpolated the H-magnitude to the model isochrone grid. Here the age is the derived age of $15.6^{+4.1}_{-3.7}$ Myr. This was done for both AMES-COND and AMES-DUSTY evolutionary models – a final mass was obtained by interpolating the $H - K_s$ colour between the two. The resulting masses are shown in Table 8. The masses derived from both models, as well as the final adopted masses of $10.4^{+0.7}_{-0.8}$ M_J and $5.3^{+0.8}_{-0.6}$ M_J for WISPIT 1b and WISPIT 1c respectively, are consistent with the planetary-mass regime.

6. Discussion

6.1. The stellar binary WISPIT 1

Our flux calibration observations revealed that WISPIT 1 is a close stellar binary. However, it shows negligible relative motion over the two-year baseline of our observations, indicating that the binarity does not significantly impact the relative astrometry of other sources in the field. This allows us to treat the system effectively as a single astrometric reference for the purpose of tracking candidate companions.

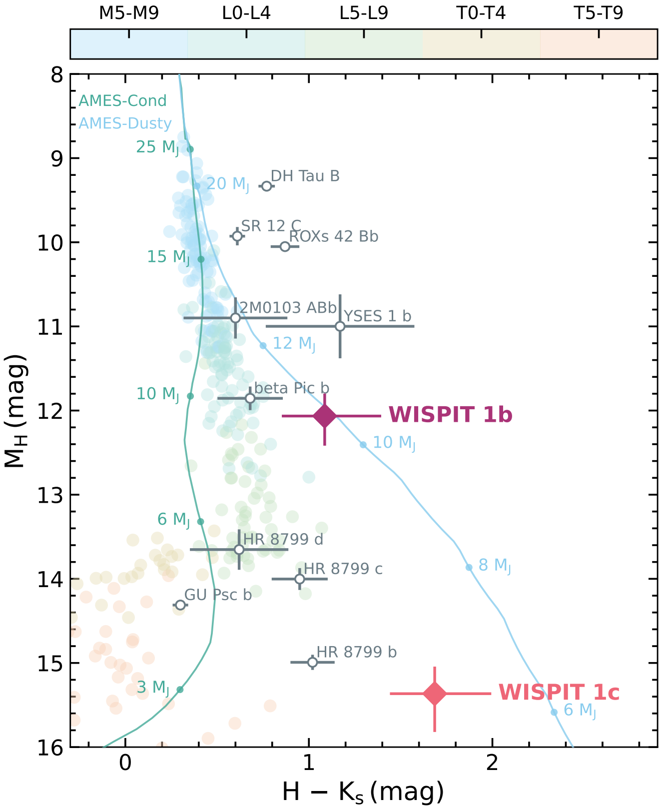

Fig. 5. Colour-magnitude diagram of WISPIT 1b and WISPIT 1c along with field brown dwarfs of various spectral types and confirmed planetary companions. Teal and cyan tracks show 15.6 Myr AMES-COND and AMES-DUSTY isochrones respectively. WISPIT 1b/WISPIT 1c are marked in purple/pink.

Table 8. Masses of WISPIT 1b and WISPIT 1c.

Model	Mass 1b (M_J)	Mass 1c (M_J)
AMES-COND	$9.24^{+0.86}_{-0.91}$	$2.91^{+0.32}_{-0.34}$
AMES-DUSTY	$10.53^{+0.65}_{-0.76}$	$6.24^{+0.67}_{-0.54}$
Interpolated	$10.4^{+0.7}_{-0.8}$	$5.3^{+0.8}_{-0.6}$

Notes. Mass estimates for both companions using AMES-COND and AMES-DUSTY evolutionary tracks. The final mass displayed in the Interpolated row is obtained by interpolating the $H - Ks$ colour between the AMES-COND and AMES-DUSTY isochrones.

We characterised the components of the WISPIT 1 system by deriving flux ratios in the H and K_s-bands, and estimated the age of the primary by comparing its $H - K_s$ colour and lithium equivalent width to the model isochrones from Žerjal et al. (2021). While we addressed the considerable cosmic scatter in lithium abundances by adopting more conservative uncertainties on the age, we acknowledge that other, unquantified sources of uncertainty remain. Uncertainties stemming from disentangling the primary's flux from that of the secondary may be underestimated, and affect both the colour and the inferred age of the star. Nevertheless, given the consistency with the age of the co-moving star, we consider the age estimate to be reasonable. High-resolution spectroscopic follow-up is required to better characterise the individual components of the binary system, and to provide a more robust constraint on its age.

6.2. Planetary companions to WISPIT 1

Both WISPIT 1b and WISPIT 1c exhibit common proper motion with WISPIT 1, which supports their interpretation as bound planetary companions. The astrometric uncertainties on WISPIT 1c, as shown in Fig. 4b, are relatively large, and the possibility that it is a background object cannot be ruled out based on the current data, but the clustering of the astrometric measurements suggest that the positional uncertainties on WISPIT 1c may be overestimated, potentially resulting from its lower S/N and the higher background RMS at this large radial separation. Follow-up observations are required to confirm its status as a bound companion.

This caution is further warranted by the recent case of YSES 2b, which was initially identified as a planetary companion to YSES 2, but with multiple SPHERE and GRAVITY epochs was later revealed to be a late type M dwarf star at a distance of over 2 kpc (Kenworthy et al. 2025). Such a scenario is a statistically unlikely event, and in the case of WISPIT 1, this improbability is further reinforced by the fact that all other background sources in the field of view are consistent with stationary background sources. It would therefore be improbable that both WISPIT 1b and WISPIT 1c are unrelated background sources that coincidentally move at the same apparent proper motion and in the same direction as WISPIT 1. Nevertheless, considering wide-separation planets exhibit little to no orbital motion over the baseline of a few years, this scenario is technically possible for all directly imaged wide-separation planets. This highlights the importance of long-term astrometric monitoring with high precision instruments such as GRAVITY.

Despite the aforementioned caveats, the current data provides considerable robust evidence that both WISPIT 1b and 1c are indeed planetary-mass companions. While the K_s-band detection of WISPIT 1c has a significance just under 5σ, making the $H - K_s$ colour and therefore the final interpolated mass somewhat uncertain, its mass derived from the H-band magnitude alone is in any case between $\sim$2.9 M_J (AMES-COND) and $\sim$6.2 M_J (AMES-DUSTY), placing it well within the planetary-mass regime. With a mass of $10.4^{+0.7}_{-0.8}$ M_J, WISPIT 1b is well below the deuterium-burning limit, and its colour is comparable to that of other directly imaged gas giants.

The large angular separation from WISPIT 1 makes both companions excellent targets for future photometric and spectroscopic follow-up observations, as this large distance limits contamination from the diffraction halo of the host star. For WISPIT 1b, atmospheric characterisations can be performed with ground-based telescopes, while WISPIT 1c, due to its faintness, would require space-based instruments such as JWST to resolve spectroscopic features. Astrometric and spectroscopic follow-up of both WISPIT 1b and 1c will be essential for conclusively validating their planetary nature and for constraining their compositions.

6.3. Comparison to other systems

The newly discovered WISPIT 1 system contributes to a growing population of wide-separation planetary systems, and shows similarities to existing systems, both in terms of system architecture and in terms of individual companion properties. As can be seen in the CMD presented in Fig. 5, WISPIT 1b's photometry is comparable to that of β Pic b (Lagrange et al. 2009). Though

WISPIT 1 may be slightly younger, both systems are roughly similar in age and the mass of WISPIT 1b is comparable to that of β Pic b (11 ± 2 M_J, Snellen & Brown 2018). However, β Pic is a more massive A-type star (e.g. Gray et al. 2006), and its companions orbit at much smaller separations. WISPIT 1b also shows striking similarities to 1RXS J160929.1-210524 b, a similar mass (7–12M_J) companion orbiting at a similar distance (~330 au) from its host star (Lafrenière et al. 2008; Ireland et al. 2011; Lachapelle et al. 2015). The star, located in the Upper Scorpius OB association, is roughly solar mass, but with an estimated age of ~5 Myr is somewhat younger than WISPIT 1. Another ~5 Myr star in that same region, GSC 06214-00210, hosts a more massive companion of 14–17 M_J at the same projected separation of ~330 au (Kraus et al. 2008; Ireland et al. 2011; Lachapelle et al. 2015). What is particularly interesting about this companion is that Bowler et al. (2011) show that its spectral features strongly hint towards the presence of a circumplanetary disk (CPD). They examined the possibility of a hypothetical scattering event by assuming it was formed much closer than its present location and was ejected to a wider orbit through a gravitational interaction with another massive body, and concluded that such an event would have likely disrupted the CPD. Hence, they interpret the retention of the disk as evidence against a past scattering event, and argue that it was likely formed in situ. While in our case, WISPIT 1b may have followed a similar formation history and could have formed in situ (e.g. by gravitational instability), it becomes increasingly difficult to explain an in situ formation for an extremely wide separation planet such as WISPIT 1c through any currently known mechanism (e.g. Veras et al. 2009; Nielsen et al. 2019).

There are not many known confirmed bound companions at projected orbital separations similar to that of WISPIT 1c, but a notable comparable object is Ross 458c, a 6–11 M_J companion orbiting at a projected separation of 1100 au from its host stars (Goldman et al. 2010; Scholz, R.-D. 2010; Burgasser et al. 2010). Although it may be more massive and could be orbiting at a larger semi-major axis than WISPIT 1c, a striking similarity between both systems is that Ross 458c also orbits a tight binary, Ross 458 AB. This binary is a M0.5 Ve + M7 Ve pair (Burgasser et al. 2010), and, with a lower limit of ~150 Myr and an upper limit of ~800 Myr, is considerably older than WISPIT 1. Various analyses of the atmosphere of Ross 458c found that it is best described by a cloudy model, and showed that best-fit models incorporated sulphide clouds or silicate clouds (Burningham et al. 2011; Morley et al. 2012; Manjavacas et al. 2019; Gaarn et al. 2023). Gaarn et al. (2023) derive a relatively high mass of 27 ± 4 M_J, well above the planetary-mass regime, leading to a correspondingly high mass ratio with its host binary, which they argue makes a planetary origin less likely. However, they also show that its C/O ratio appears to be notably higher than that of its primaries and argue that this may suggest a planetary formation route for Ross 458c, followed by outward migration to its current position. In the case of WISPIT 1c, its lower mass-ratio with the binary, combined with the presence of both a stellar binary companion and another planetary companion in the system, makes a similar formation scenario – initial formation closer in, followed by scattering to a wide orbit – a plausible origin.

Another system that is structurally analogous in several respects is YSES 1 (Bohn et al. 2020a; Bohn et al. 2020b), a young solar-type star that also hosts two directly imaged planetary companions. Its estimated temperature of 4590 ± 50 K and age of 15 ± 5 Myr (Bohn et al. 2020a) are comparable to those of the primary of WISPIT 1. The colours and masses of the planets are also similar: WISPIT 1b is approximately 4 M_J less massive than YSES 1b and WISPIT 1c is roughly 2 M_J less massive than YSES 1c. Zhang et al. (2024) found that the C/O ratio of YSES 1b is consistent with that of YSES 1, and argue that this may suggest (in situ) formation via gravitational instability or core accretion beyond the snowline. For YSES 1c, they derived the C/O ratio to be either solar, consistent with in situ formation similar to YSES 1b, or sub-solar, consistent with formation within the CO iceline followed by outward scattering. The YSES 1 planets have been reported to show silicate features in their atmospheres, and a CPD has been directly detected around YSES 1b (Hoch et al. 2025). As in the case of GSC 06214-00210b, if the CPD was formed during planet formation, it could further support the hypothesis of in situ formation for YSES 1b. Zhang et al. (2024) also argue that, given its low mass, YSES 1c is more likely to have formed closer to the star via bottom-up formation and was subsequently scattered outward to its current position. This prompts the intriguing question of whether the two known planets in the system may have distinct formation pathways. Given the similarities to the YSES 1 system, this raises the possibility that perhaps the WISPIT 1 planets, too, may have formed through different formation pathways.

6.4. Wide-separation circumbinary planets

While circumbinary planets are much more rare than planets orbiting single stars, there are a few notable examples that share similarities with the WISPIT 1 system. A circumbinary planet similar in mass to WISPIT 1b is b Cen (AB)b, a 10.9 ± 1.6 M_J planet orbiting at 556 ± 17 au from b Cen AB (Janson et al. 2021). Although with a mass of 6–10 M_J, the central pair is considerably more massive than that of WISPIT 1. It is of a similar age, and like WISPIT 1, it was never part of any very high density environment. The latter lowers the probability of gravitational capture scenarios, which was estimated to be approximately 17% for b Cen (AB)b (Janson et al. 2021). While scattering caused by the binary remains a possibility, the low eccentricity of b Cen (AB)b favours formation close to its present location, most likely due to gravitational instability processes. Scattering is considered to be the more viable option for HD 106906 b (Bailey et al. 2014), an 11 M_J circumbinary planet located at a projected physical separation of approximately 737 au from its host. Similar to WISPIT 1, HD 106906 is a ~15 Myr system that was initially thought to be a single star but was later revealed to be a close binary (Lagrange et al. 2016). With a total stellar mass of at least 2.5 $M_\odot$, this places its companion at a mass ratio close to that of WISPIT 1c. Various formation mechanisms have been put forward for this planet, with suggestions of planet-capture, as well as in situ formation through gravitational instability and formation closer in followed by outward scattering to a wider orbit. While the relatively low eccentricity of 0.4 (Nguyen et al. 2020) would seem to favour in situ formation, simulations from Rodet et al. (2017) show that this configuration can be reproduced if the orbit of the companion scattered outward through interaction with the binary is stabilised by interaction with its own circumstellar disk, or by an external perturber through a flyby. Conversely, Moore et al. (2023) argue that the companion was most likely initially in a stable orbit and was instead scattered to its current configuration by a flyby with a free-floating planet. These examples illustrate that wide-orbit circumbinary planets may arise through various pathways, with both in situ formation and formation closer to the stars followed by outward scattering remaining viable under certain conditions. The similarities between these systems, in particular the wide-separation of the companions, suggest that the presence of a binary may play a role in the formation of such systems.

With a projected physical separation of at least 338 au, WISPIT 1b ranks among the top 10 widest-separation exoplanets with masses below 13 M_J; at 840 au, WISPIT 1c currently ranks seventh[7]. An interesting trend is that, of the ten currently known widest-separation ($\gtrsim$350 au) exoplanets, six (Burgasser et al. 2010; Bailey et al. 2014; Dupuy et al. 2018; Janson et al. 2021; Dupuy et al. 2023; Rothermich et al. 2024) orbit a stellar multiple system. In contrast, among all exoplanets with a reported semi-major axis, fewer than 20% orbit stellar multiples – a fraction that remains approximately the same when considering only directly imaged planets. Although the sample size is too small to allow for any definitive statistical conclusions, this trend raises the question of whether dynamical interactions in multiple systems may have played a role in forming companions at or scattering companions to such wide separations. These objects might represent a distinct population of wide-separation giant planets; future large-scale surveys and discoveries will be essential to better understand their formation pathways and dynamical evolution.

7. Conclusions

In this paper we present the detection and characterisation of two co-moving planetary companions to a young stellar binary. Based on lithium depletion isochrones, we derived the age of the primary to be $15.6^{+4.1}_{-3.7}$ Myr. Using theoretical evolutionary models to convert the distance and photometry into luminosity and adopting this age estimate, the masses of the two companions are $10.4^{+1.1}_{-0.8}$ M_J and $5.3^{+1.1}_{-0.6}$ M_J at projected physical separations of 338 au and 840 au, respectively. The astrometry across three epochs is inconsistent with a distant background source. No orbital motion of the companions around the central binary is detected, within the errors on the measured astrometry.

Various formation pathways are possible for both planets, from in situ formation via gravitational instability, to formation closer in followed by outward scattering, to planet-capture scenarios. Constraining these possibilities requires detailed follow-up of their atmospheric chemistries and precise astrometric monitoring to determine their orbital periods and eccentricities. Future work includes deeper photometry and spectroscopy of both planets to confirm their low mass and low gravity and potentially measure their rotation period. Astrometric monitoring, especially of WISPIT 1b, with high precision instruments such as GRAVITY will help determine their orbital parameters. Deeper ground based observations from large telescopes will enable searches for additional companions in the system, and JWST will be able to detect wider separation sub-Jupiter mass companions. Together, these measurements will constrain the range of viable formation models for these exoplanets.

Acknowledgements. This publication makes use of VOSA, developed under the Spanish Virtual Observatory (`https://svo.cab.inta-csic.es`) project funded by MCIN/AEI/10.13039/501100011033/ through grant PID2020-112949GB-I00. VOSA has been partially updated by using funding from the European Union's Horizon 2020 Research and Innovation Programme, under Grant Agreement nº 776403 (EXOPLANETS-A). This research has used the SIMBAD database, operated at CDS, Strasbourg, France (Wenger et al. 2000). This work has used data from the European Space Agency (ESA) mission *Gaia* (`https://www.cosmos.esa.int/gaia`), processed by the *Gaia* Data Processing and Analysis Consortium (DPAC, `https://www.cosmos.esa.int/web/gaia/dpac/consortium`). Funding for the DPAC has been provided by national institutions, in particular the institutions participating in the *Gaia* Multilateral Agreement. This research has made use of NASA's Astrophysics Data System. Part of this research was carried out at the Jet Propulsion Laboratory, California Institute of Technology, under a contract with the National Aeronautics and Space Administration (80NM0018D0004). This research made use of SAOImageDS9, a tool for data visualization supported by the Chandra X-ray Science Center (CXC) and the High Energy Astrophysics Science Archive Center (HEASARC) with support from the JWST Mission office at the Space Telescope Science Institute for 3D visualization (Joye & Mandel 2003). The authors thank the anonymous reviewer for their swift and helpful feedback to this publication. To achieve the scientific results presented in this article we made use of the *Python* programming language[8], including the *SciPy* (Virtanen et al. 2020), *NumPy* (Harris et al. 2020), *Matplotlib* (Hunter 2007), *emcee* (Foreman-Mackey et al. 2013), *astropy* (Astropy Collaboration 2013, 2018, 2022), *backtracks* (Balmer et al. 2025) and *PynPoint* (Amara & Quanz 2012; Stolker et al. 2019).

References

Allard, F., Hauschildt, P. H., Alexander, D. R., Tamanai, A., & Schweitzer, A. 2001, ApJ, 556, 357
Allard, F., Homeier, D., Freytag, B., Schaffenberger, W., & Rajpurohit, A. S. 2013, Mem. Soc. Astron. It. Suppl., 24, 128
Amara, A., & Quanz, S. P. 2012, MNRAS, 427, 948
Astropy Collaboration (Robitaille, T. P., et al.) 2013, A&A, 558, A33
Astropy Collaboration (Price-Whelan, A. M., et al.) 2018, AJ, 156, 123
Astropy Collaboration (Price-Whelan, A. M., et al.) 2022, ApJ, 935, 167
Bailer-Jones, C. A. L., Rybizki, J., Fouesneau, M., Demleitner, M., & Andrae, R. 2021, AJ, 161, 147
Bailey, V., Meshkat, T., Reiter, M., et al. 2014, ApJ, 780, L4
Balmer, W. O., Otten, G. P. P. L., & Stolker, T. 2025, `https://doi.org/10.5281/zenodo.14838370`
Bayo, A., Rodrigo, C., Barrado Y Navascués, D., et al. 2008, A&A, 492, 277
Beccari, G., Boffin, H. M. J., Jerabkova, T., et al. 2018, MNRAS, 481, L11
Beuzit, J. L., Vigan, A., Mouillet, D., et al. 2019, A&A, 631, A155
Biller, B. A., & Bonnefoy, M. 2018, Exoplanet Atmosphere Measurements from Direct Imaging, eds. H. J. Deeg, & J. A. Belmonte (Cham: Springer International Publishing), 2107
Bohn, A. J., Kenworthy, M. A., Ginski, C., et al. 2019, A&A, 624, A87
Bohn, A. J., Kenworthy, M. A., Ginski, C., et al. 2020a, MNRAS, 492, 431
Bohn, A. J., Kenworthy, M. A., Ginski, C., et al. 2020b, ApJ, 898, L16
Bohn, A. J., Ginski, C., Kenworthy, M. A., et al. 2021, A&A, 648, A73
Boller, T., Freyberg, M. J., Trümper, J., et al. 2016, A&A, 588, A103
Boss, A. P. 1997, Science, 276, 1836
Bowler, B. P., & Nielsen, E. L. 2018, Occurrence Rates from Direct Imaging Surveys (CUP), 155
Bowler, B. P., Liu, M. C., Kraus, A. L., Mann, A. W., & Ireland, M. J. 2011, ApJ, 743, 148
Buder, S., Asplund, M., Duong, L., et al. 2018, MNRAS, 478, 4513
Buder, S., Sharma, S., Kos, J., et al. 2021, MNRAS, 506, 150
Burgasser, A. J., Simcoe, R. A., Bochanski, J. J., et al. 2010, ApJ, 725, 1405
Burningham, B., Leggett, S. K., Homeier, D., et al. 2011, MNRAS, 414, 3590
Carbillet, M., Bendjoya, P., Abe, L., et al. 2011, Exp. Astron., 30, 39
Chabrier, G., Baraffe, I., Allard, F., & Hauschildt, P. 2000, ApJ, 542, 464
Chauvin, G., Desidera, S., Lagrange, A. M., et al. 2017, A&A, 605, L9
Claudi, R., & Mesa, D. 2024, Galaxies, 13, 3
Currie, T., Kuzuhara, M., Chilcote, J., et al. 2025, AAS Meeting Abstracts, 245, 175.03
Cutri, R. M., & et al. 2012, VizieR Online Data Catalog: WISE All-Sky Data Release (Cutri+ 2012), VizieR On-line Data Catalog: II/311
Cutri, R. M., Skrutskie, M. F., van Dyk, S., et al. 2003, 2MASS All Sky Catalog of point sources (IPAC)
Cutri, R. M., Wright, E. L., Conrow, T., et al. 2013, Explanatory Supplement to the AllWISE Data Release Products, Explanatory Supplement to the AllWISE Data Release Products, by R. M. Cutri et al.
de Zeeuw, P. T., Hoogerwerf, R., de Bruijne, J. H. J., Brown, A. G. A., & Blaauw, A. 1999, AJ, 117, 354
Delorme, P., Chomez, A., Squicciarini, V., et al. 2024, A&A, 692, A263
Dodson-Robinson, S. E., Veras, D., Ford, E. B., & Beichman, C. A. 2009, ApJ, 707, 79
Dohlen, K., Langlois, M., Saisse, M., et al. 2008, SPIE Conf. Ser., 7014, 70143L
Dopita, M., Hart, J., McGregor, P., et al. 2007, Astrophys. Space Sci., 310, 255
Dupuy, T. J., Liu, M. C., Allers, K. N., et al. 2018, AJ, 156, 57

---

[7] Retrieved from the NASA Exoplanet Archive on July 10, 2025: `https://exoplanetarchive.ipac.caltech.edu/`

[8] Python Software Foundation, `https://www.python.org/`

Dupuy, T. J., Liu, M. C., Evans, E. L., et al. 2023, MNRAS, 519, 1688
El Morsy, M., Currie, T., Kuzuhara, M., et al. 2024, arXiv e-prints [arXiv:2409.06773]
Epchtein, N., Deul, E., Derriere, S., et al. 1999, A&A, 349, 236
Follette, K. B. 2023, PASP, 135, 093001
Foreman-Mackey, D., Hogg, D. W., Lang, D., & Goodman, J. 2013, PASP, 125, 306
Forgan, D. H., Hall, C., Meru, F., & Rice, W. K. M. 2018, MNRAS, 474, 5036
Franson, K., Bowler, B. P., Zhou, Y., et al. 2023, ApJ, 950, L19
Freund, S., Czesla, S., Predehl, P., et al. 2024, A&A, 684, A121
Fusco, T., Rousset, G., Sauvage, J. F., et al. 2006, Optics Exp., 14, 7515
Fusco, T., Sauvage, J. F., Petit, C., et al. 2014, SPIE Conf. Ser., 9148, 91481U
Gaarn, J., Burningham, B., Faherty, J. K., et al. 2023, MNRAS, 521, 5761
Gaia Collaboration (Brown, A. G. A., et al.) 2021, A&A, 649, A1
Goldman, B., Marsat, S., Henning, T., Clemens, C., & Greiner, J. 2010, MNRAS, 405, 1140
Gray, R. O., Corbally, C. J., Garrison, R. F., et al. 2006, AJ, 132, 161
Green, M. J., Maoz, D., Mazeh, T., et al. 2023, MNRAS, 522, 29
Harris, C. R., Millman, K. J., van der Walt, S. J., et al. 2020, Nature, 585, 357
Heiles, C. 1998, ApJ, 498, 689
Henden, A. A., Templeton, M., Terrell, D., et al. 2016, VizieR Online Data Catalog: AAVSO Photometric All Sky Survey (APASS) DR9 (Henden+, 2016), VizieR On-line Data Catalog: II/336
Hoch, K. K. W., Rowland, M., Petrus, S., et al. 2025, Nature, 643, 938
Hunter, J. D. 2007, Comput. Sci. Eng., 9, 90
Ireland, M. J., Kraus, A., Martinache, F., Law, N., & Hillenbrand, L. A. 2011, ApJ, 726, 113
Janson, M., Gratton, R., Rodet, L., et al. 2021, Nature, 600, 231
Joye, W. A., & Mandel, E. 2003, ASP Conf. Ser., 295, 489
Kenworthy, M., Stolker, T., Kammerer, J., et al. 2025, A&A, https://doi.org/10.1051/0004-6361/202556170
Kenworthy, M. A., & Haffert, S. Y. 2025, ARA&A, 63, 179
Kerr, R. M. P., Rizzuto, A. C., Kraus, A. L., & Offner, S. S. R. 2021, ApJ, 917, 23
Kratter, K., & Lodato, G. 2016, ARA&A, 54, 271
Kraus, A. L., Ireland, M. J., Martinache, F., & Lloyd, J. P. 2008, ApJ, 679, 762
Kroupa, P. 2001, MNRAS, 322, 231
Lachapelle, F.-R., Lafrenière, D., Gagné, J., et al. 2015, ApJ, 802, 61
Lafrenière, D., Doyon, R., Marois, C., et al. 2007, ApJ, 670, 1367
Lafrenière, D., Jayawardhana, R., & van Kerkwijk, M. H. 2008, ApJ, 689, L153
Lagrange, A.-M., Gratadour, D., Chauvin, G., et al. 2009, A&A, 493, L21
Lagrange, A. M., Langlois, M., Gratton, R., et al. 2016, A&A, 586, L8
Lagrange, A. M., Rubini, P., Nowak, M., et al. 2020, A&A, 642, A18
Lallement, R., Vergely, J. L., Valette, B., et al. 2014, A&A, 561, A91
Lambrechts, M., & Johansen, A. 2012, A&A, 544, A32
Macintosh, B., Graham, J. R., Ingraham, P., et al. 2014, Proc. Natl. Acad. Sci., 111, 12661
Macintosh, B., Graham, J. R., Barman, T., et al. 2015, Science, 350, 64
MacKay, D. J. C. 2003, Information Theory, Inference, and Learning Algorithms (Cambridge: Cambridge University Press)
Mainzer, A., Bauer, J., Cutri, R. M., et al. 2014, ApJ, 792, 30
Maire, A.-L., Langlois, M., Dohlen, K., et al. 2016, SPIE Conf. Ser., 9908, 990834
Maire, A.-L., Langlois, M., Delorme, P., et al. 2021, J. Astron. Teles. Instrum. Syst., 7, 035004
Manjavacas, E., Apai, D., Lew, B. W. P., et al. 2019, ApJ, 875, L15
Marois, C., Macintosh, B., Barman, T., et al. 2008, Science, 322, 1348
Marois, C., Zuckerman, B., Konopacky, Q. M., Macintosh, B., & Barman, T. 2010, Nature, 468, 1080
Mawet, D., Milli, J., Wahhaj, Z., et al. 2014, ApJ, 792, 97
Mendigutía, I., Solano, E., Vioque, M., et al. 2022, A&A, 664, A66
Merloni, A., Lamer, G., Liu, T., et al. 2024, A&A, 682, A34
Moore, N. W. H., Li, G., Hassenzahl, L., et al. 2023, ApJ, 943, 6
Mordasini, C., Alibert, Y., & Benz, W. 2009a, A&A, 501, 1139
Mordasini, C., Alibert, Y., Benz, W., & Naef, D. 2009b, A&A, 501, 1161
Mordasini, C., Alibert, Y., Benz, W., Klahr, H., & Henning, T. 2012, A&A, 541, A97
Morley, C. V., Fortney, J. J., Marley, M. S., et al. 2012, ApJ, 756, 172
Nguyen, M. M., De Rosa, R. J., & Kalas, P. 2020, AJ, 161, 22
Nielsen, E. L., De Rosa, R. J., Macintosh, B., et al. 2019, AJ, 158, 13
Nowak, M., Lacour, S., Lagrange, A. M., et al. 2020, A&A, 642, L2
O'Neill, T. J., Zucker, C., Goodman, A. A., & Edenhofer, G. 2024, ApJ, 973, 136
Paunzen, E., Netopil, M., Prišegen, M., & Faltová, N. 2024, A&A, 689, A270
Pecaut, M. J., & Mamajek, E. E. 2013, ApJS, 208, 9
Pecaut, M. J., & Mamajek, E. E. 2016, MNRAS, 461, 794
Pollack, J. B., Hubickyj, O., Bodenheimer, P., et al. 1996, Icarus, 124, 62
Rodet, L., Beust, H., Bonnefoy, M., et al. 2017, A&A, 602, A12
Rothermich, A., Faherty, J. K., Bardalez-Gagliuffi, D., et al. 2024, AJ, 167, 253
Schlafly, E. F., & Finkbeiner, D. P. 2011, ApJ, 737, 103
Schlegel, D. J., Finkbeiner, D. P., & Davis, M. 1998, ApJ, 500, 525
Scholz, R.-D. 2010, A&A, 515, A92
Snellen, I. A. G., & Brown, A. G. A. 2018, Nat. Astron., 2, 883
Soummer, R. 2005, ApJ, 618, L161
Stassun, K. G., Oelkers, R. J., Paegert, M., et al. 2019, AJ, 158, 138
Stolker, T., Bonse, M. J., Quanz, S. P., et al. 2019, A&A, 621, A59
Stolker, T., Quanz, S. P., Todorov, K. O., et al. 2020, A&A, 635, A182
Stolker, T., Samland, M., Waters, L. B. F. M., et al. 2025, A&A, 700, A21
Veras, D., Crepp, J. R., & Ford, E. B. 2009, ApJ, 696, 1600
Vigan, A., Bonavita, M., Biller, B., et al. 2017, A&A, 603, A3
Vigan, A., Fontanive, C., Meyer, M., et al. 2021, A&A, 651, A72
Virtanen, P., Gommers, R., Oliphant, T. E., et al. 2020, Nat. Methods, 17, 261
Voges, W., Aschenbach, B., Boller, T., et al. 2000, IAU Circ., 7432, 3
Žerjal, M., Rains, A. D., Ireland, M. J., et al. 2021, MNRAS, 503, 938
Wenger, M., Ochsenbein, F., Egret, D., et al. 2000, A&AS, 143, 9
Zari, E., Hashemi, H., Brown, A. G. A., Jardine, K., & de Zeeuw, P. T. 2018, A&A, 620, A172
Zhang, Z., Liu, M. C., Claytor, Z. R., et al. 2021, ApJ, 916, L11
Zhang, Y., González Picos, D., de Regt, S., et al. 2024, AJ, 168, 246

Appendix A: Median combined observations

The median combined observations from 2022, 2023, and 2024, with all detected sources in the field of view annotated, are shown in Figs. A.1, A.2 and A.3, respectively. Of the *H*-band observations, the 2023 epoch (Fig. A.2) has better reported observing conditions and AO correction compared to 2022 (Fig. A.1), resulting in a higher S/N for sources closer to the star, such as WISPIT 1b. However, the 2023 observation visually appears noisier overall, either due to increased detector noise or atmospheric effects. This is reflected in the background RMS, which is notably higher at larger radial separations in the 2023 data compared to 2022. Consequently, background-limited sources farther from the star, such as WISPIT 1c, have a slightly better S/N in the 2022 epoch. The 2024 K_s-band observation (Fig. A.3) was taken under reasonably good observing conditions, but show a thermal background pattern affecting the lower half of the frame. Since WISPIT 1c is near this region, its measured flux is strongly affected, and the local background estimate becomes less reliable, resulting in a low-S/N detection.

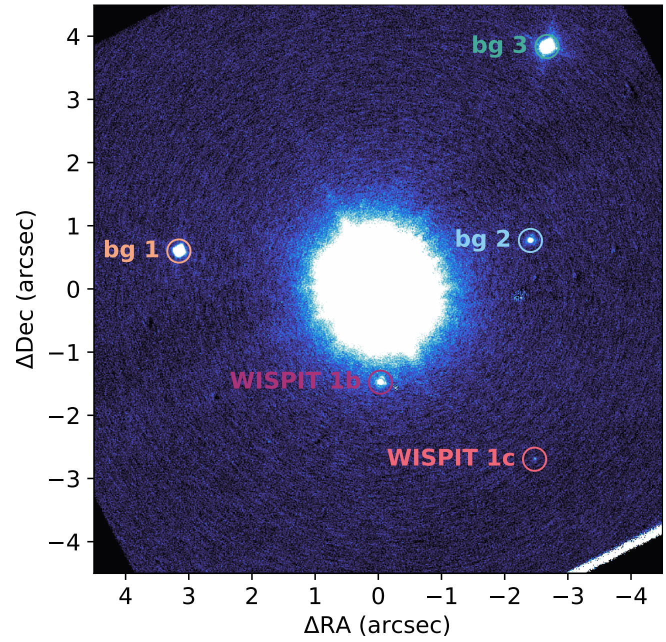

Fig. A.1: WISPIT 1b, 1c, and background sources highlighted in the *H*-band median-combined image of epoch 2022-11-19.

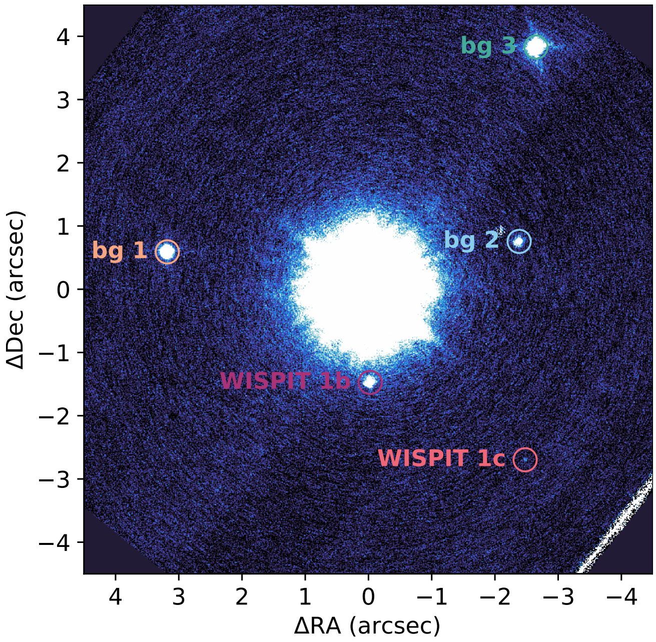

Fig. A.2: WISPIT 1b, 1c, and background sources highlighted in the *H*-band median-combined image of epoch 2023-12-03.

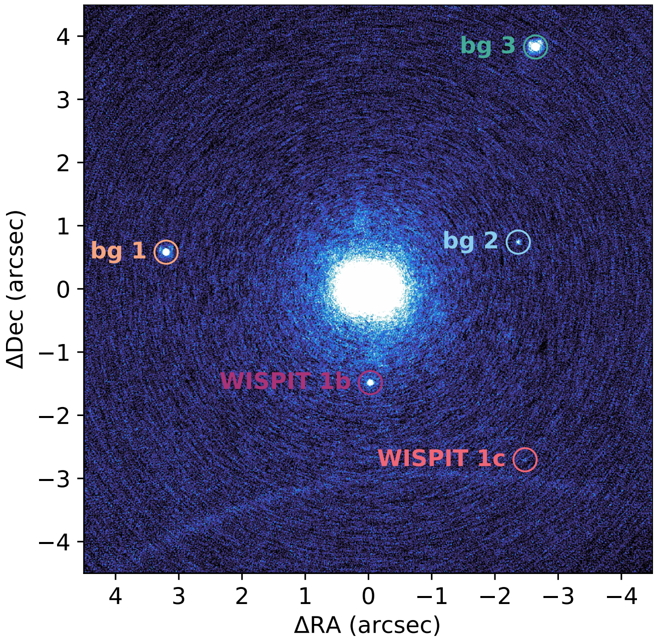

Fig. A.3: WISPIT 1b, 1c, and background sources highlighted in the K_s-band median-combined image of epoch 2024-11-30.

Appendix B: Environs of WISPIT 1

The star has not been previously assigned membership to any stellar groups, but we discuss its environs. WISPIT 1 is ~4° SW of the Vel OB2 association (alias: Collinder 173) (e.g. de Zeeuw et al. 1999); however, its members are more distant and have smaller proper motions ($\varpi = 2.85 \pm 0.08$ mas, $d \simeq 351 \pm 10$ pc, $\mu_\alpha,\ \mu_\delta\ =\ -6.20 \pm 0.44,\ 9.08 \pm 0.64$ mas yr^{-1}; Beccari et al. 2018; Mendigutía et al. 2022). Beccari et al. (2018) finds Vel OB2 to have six subclusters with a range of ages of 10-30 Myr, including two well-studied clusters (γ Vel, NGC 2547) and four new subgroups. WISPIT 1 is 1°.5 away from the Vel OB2 subgroup [BBJ2018] 2; however, its distance and proper motion again differ significantly from the star: (ϖ = 2.42 ± 0.05 mas, $d \simeq 413 \pm 8$ pc, μ_α, μ_δ = −5.41 ± 0.19, 8.18 ± 0.15 mas yr^{-1}; Beccari et al. 2018), with the distances differing by ∼184 pc, and tangential velocities differing by ∼17 km s^{-1} at the distance of WISPIT 1. We conclude that despite WISPIT 1's projected proximity to Vel OB2 and its subgroups, its distance and kinematics are inconsistent with membership to that complex.

A neighbouring star with a separation of 111" appears to share the proper motion and parallax of WISPIT 1. 2MASS J07512310-5008109 (UCAC4 200-015609, Gaia DR3 5517037503494641024, GALAH 151231003201128) is a Li-rich star in the GALAH survey (Buder et al. 2018, 2021), with detectable X-ray emission in the ROSAT and eROSITA X-ray All-Sky Surveys (1RXS J075123.3-500756, 2RXS J075123.1-500754, 1eRASS J075122.9-500810; Voges et al. 2000; Boller et al. 2016; Merloni et al. 2024; Freund et al. 2024). Naturally, the star appears to be fast-rotating, with the GALAH survey reporting $v \sin i$ = 20.812 ± 1.018 km s^{-1} (Buder et al. 2018), and Green et al. (2023) estimated $P_{\rm rot}$ = 5.47 d using TESS time series photometry. Using Gaia DR3 astrometry and epoch 2016.0 positions, we estimate 2MASS J07512310-5008109 to be at separation ρ = 109.886066 ± 0.000022 arcsec and PA = 87°.420226 with respect to WISPIT 1, translating to projected separation Δ = 25147 au at d = 229 pc. Their proper motions differ by $\Delta\mu_\alpha$, $\Delta\mu_\delta$ = 0.283 ± 0.020, 2.465 ± 0.021 mas yr^{-1}, which at d = 229 pc translates to difference in tangential velocities of ΔV_α, ΔV_δ = 0.307 ± 0.022, 2.674 ± 0.023 km s^{-1}. The Gaia DR3 parallaxes for WISPIT 1 and 2MASS J07512310-5008109 are in remarkable agreement – within 1.45σ ($\Delta\varpi = 0.0246 \pm 0.0170$ mas), and their inferred Gaia DR3 distances differ by only Δd = 0.356 ± 0.810 pc (Bailer-Jones et al. 2021). 2MASS J07512310-5008109 is brighter (G = 11.72, V = 11.91) than WISPIT 1 (G = 12.72, V = 13.15), and hotter ($T_{\rm eff} \simeq 5730$ K; Gaia Collaboration 2021) so we suspect that 2MASS J07512310-5008109 may be the primary of this system. Another very faint and very red co-moving co-distant star in Zari et al. (2018) is 2MASS J07485619-4656229. This star has a parallax of ϖ = 4.43 ± 0.08 mas ($d \simeq 227 \pm 8$ pc) and a proper motion of μ_α, μ_δ = −20.766 ± 0.096, 16.099 ± 0.098 mas yr^{-1}. The age assigned to this star by Kerr et al. (2021) is $16.8^{+3.5}_{-3.9}$ Myr.

Appendix C: Reddening towards WISPIT 1

Gaia DR3 quotes unusually high reddening and extinction estimates for WISPIT 1: $A_0 = 1.4306^{+0.0030}_{-0.0033}$ mag, $A_G = 1.1341^{+0.0025}_{-0.0027}$ mag, $E(B_p - R_p) = 0.6128^{+0.0014}_{-0.0016}$. These are unexpected as WISPIT 1 does not appear to be projected towards a particularly dusty region, and the maximum reddening expected from interstellar dust is predicted to be $E(B-V)_{max}$ = 0.2160 ± 0.0162 ($A_{V max}$ = 0.6482 mag) based on the dust maps from Schlafly & Finkbeiner (2011)[9]. Given the importance of extinction to the assessment of the intrinsic colours, effective temperatures, luminosities, and inferred ages for WISPIT 1 and its companions, we investigate the reddening in more detail.

To get an idea of the expected reddening due to interstellar medium towards WISPIT 1, we queried the E $(B-V)$ reddening values for stars from Paunzen et al. (2024), and cross-reference their 2MASS IDs with SIMBAD to assign parallaxes (usually from Gaia DR3) and inferred distances. In Fig. C.1, we plot the distances of stars within 2° of WISPIT 1 (calculated as $d = 1/\varpi$) with E $(B-V)$ values in the Paunzen et al. (2024) catalog. The general trend of reddening in the direction of WISPIT 1 can be characterised as follows: (i) negligible reddening within $d \lesssim 265$ pc, with – at most – a reddening trend of $\Delta E(B-V)/\Delta d$ ≃ 0.06 mag kpc^{-1}. (ii) A "wall" of reddening $\Delta E(B-V) \simeq 0.05$ mag at $d \simeq 265$ pc, beyond which all of the neighbouring stars have at least $E(B-V) \geq 0.07$ mag. (iii) Another low-density region at distances ∼265 pc $\lesssim d \lesssim$ 50 with similar reddening slope, followed by a region of larger E $(B-V)$ reddening values (∼0.1-0.3 mag) with large scatter beyond $d > 450$ pc.

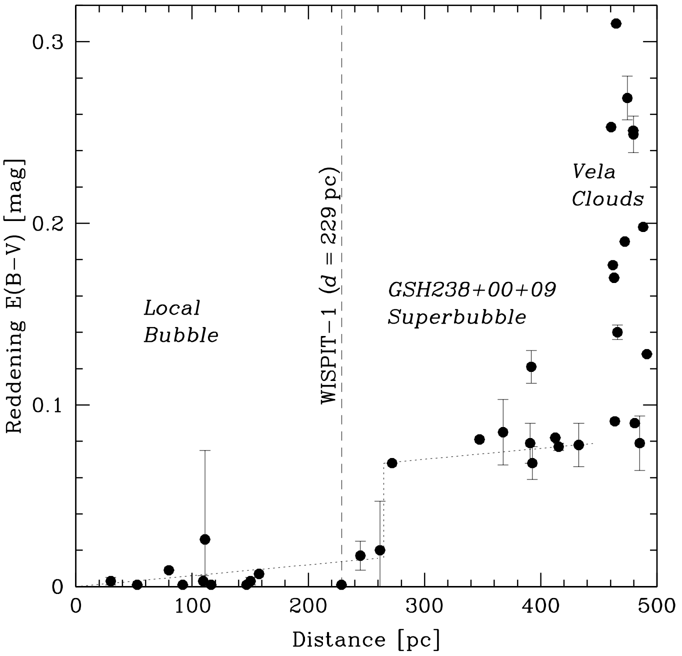

Fig. C.1: Distance versus reddening E $(B-V)$ for stars within 2° of WISPIT 1. Distances are calculated as $d = 1/\varpi$ from the default parallaxes in SIMBAD, and the reddening E $(B-V)$ values are the mean values provided by Paunzen et al. (2024). The long-dashed vertical list corresponds to the distance to WISPIT 1 (d = 229 pc), and the dotted lines are fiducial E $(B-V)$ reddening slopes of 0.06 mag kpc^{-1} up to distance $d \simeq 265$ pc, where there is a E $(B-V) \simeq 0.05$ mag wall of reddening at the interface between the Local Bubble and GSH238+00+09 Super-Bubble (Heiles 1998; Lallement et al. 2014; O'Neill et al. 2024).

A larger scale view of the 3D reddening can be viewed in Fig. 1 of Lallement et al. (2014), where WISPIT 1 (ℓ, b = 263°.70, -11°.71, d = 229 pc) sits at (X, Y ≃ -25, -224 pc). On the scales of tens of degrees, the Local Bubble was previously known to stretch to $d \simeq$ 200-300 pc in the general direction of WISPIT 1 (e.g. Fig. 3 of O'Neill et al. 2024). The "wall" of reddening E $(B-V)$ ≃ 0.05 mag at $d \simeq 265$ pc appears to be the interface between the Local Bubble and the GSH238+00+09 super-bubble (Heiles 1998; Lallement et al. 2014). The Paunzen et al. (2024) catalog contains some neighbouring hot stars at similar distances as WISPIT 1 with very small reddenings, e.g. the B9V star HD 66192 (2MASS J08000557-4854195, 114' away, d = 228 pc) with $E(B-V)$ = 0.001 mag, the B2V star HD 64740 (2MASS J07530364-4936469, 36' away, d = 245 pc) with $E(B-V)$ = 0.017 ± 0.008 mag, the F2III/IV star HD 63176 (2MASS J07450716-5017163, 59' away, d = 262 pc) with $E(B-V)$ = 0.027 ± 0.027 mag. The TIC (Stassun et al. 2019) predicts $E(B-V)$ = 0.0674 ± 0.0103 mag based on a very simple model assuming an exponential model of disk reddening and

---

[9] Queried via the Galactic Dust Reddening and Extinction tool at IRSA `https://irsa.ipac.caltech.edu/applications/DUST/`, with the mean and rms based on pixels within 5' radius.

maximum reddening informed by the Schlegel et al. (1998) dust maps, but the estimated value seems too high (more appropriate for $d > 275$ pc stars) and does not account for the obvious bubbles and their interfaces observed in the reddening estimates (e.g. Fig. 1). So we discount the TIC reddening estimate. The trend seen among the neighbouring stars with Paunzen et al. (2024) reddening estimates suggests that WISPIT is just within the inner edge of the Local Bubble with interstellar reddening of approximately $E(B-V) \simeq 0.015 \pm 0.015$ mag ($A_V \simeq 0.047 \pm 0.047$ mag). We conclude that WISPIT 1 lies within the Local Bubble, and there is no evidence for large-scale interstellar dust in the 3D vicinity or foreground of WISPIT 1 that can account for the large reddenings and extinctions quoted by Gaia Collaboration (2021).

Appendix D: Apparent magnitude decomposition

To derive the apparent magnitudes of the primary and secondary stars from the observed 2MASS system magnitudes, we convert 2MASS total magnitudes to fluxes, apply the measured flux ratios, and convert back to magnitudes. In the derivation included below, $H_{\rm tot}$ and $K_{s,\rm tot}$ denote the total magnitudes from Table 1, and R_H, R_{K_s} the secondary-to-primary flux ratios in each band. The primary is denoted with A and the secondary with B. The associated uncertainties are computed with standard error propagation of the uncertainties in the flux ratio and the 2MASS magnitudes.

Primary:
$$F_H^A = \frac{10^{-0.4H_{\rm tot}}}{1+R_H}, \qquad F_{K_s}^A = \frac{10^{-0.4K_{s,\rm tot}}}{1+R_{K_s}},$$
$$H_A = -2.5\log_{10}(F_H^A), \quad K_{s,A} = -2.5\log_{10}(F_{K_s}^A).$$

Secondary:
$$F_H^B = 10^{-0.4H_{\rm tot}} - F_H^A, \qquad F_{K_s}^B = 10^{-0.4K_{s,\rm tot}} - F_{K_s}^A,$$
$$H_B = -2.5\log_{10}(F_H^B), \quad K_{s,B} = -2.5\log_{10}(F_{K_s}^B).$$

Appendix E: Lithium isochrones

Fig. E.1 shows lithium equivalent width as a function of $H-K_s$ colour for various stellar ages. Note that the flux at the Li I line (6708 Å) is dominated by the primary star; the much fainter and cooler secondary star is not expected to contribute to the lithium absorption measurement.

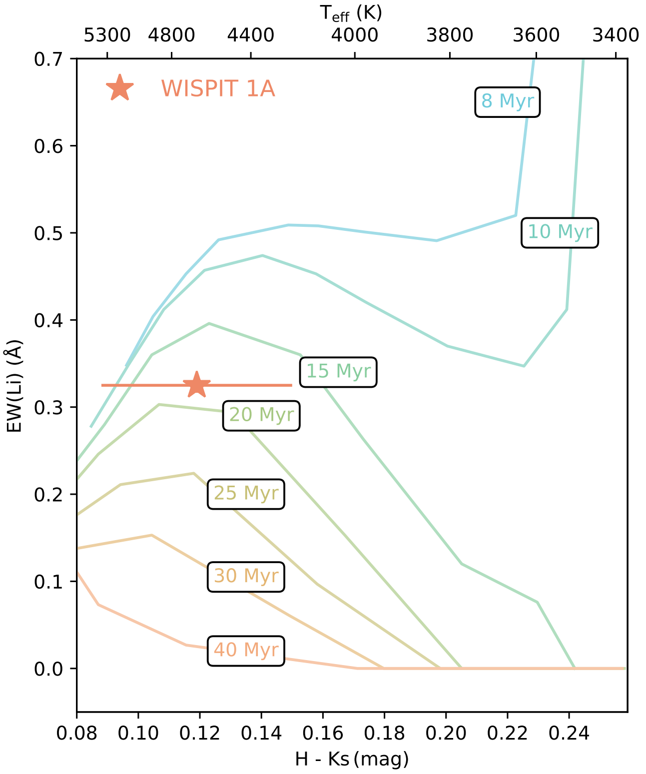

Fig. E.1: Lithium isochrones from Žerjal et al. (2021) adapted to $H-K_s$. WISPIT 1A is indicated with an orange star.

Appendix F: Proper motion of background objects

Fig. F.1 presents the measured positions of the background sources within the field of view, along with predicted background tracks for stationary background objects. It is evident from this figure that the astrometry of these sources is consistent with stationary background objects, which strengthens the interpretation of WISPIT 1b and WISPIT 1c as co-moving planetary companions, since they clearly deviate from these predicted tracks. We note, however, that the third epoch position of background object 3 does not follow the expected trajectory. Although it is possible that it is a non-stationary background source, another possible explanation is that this source may be a binary, as its PSF visually slightly deviates from that of a single point-source.

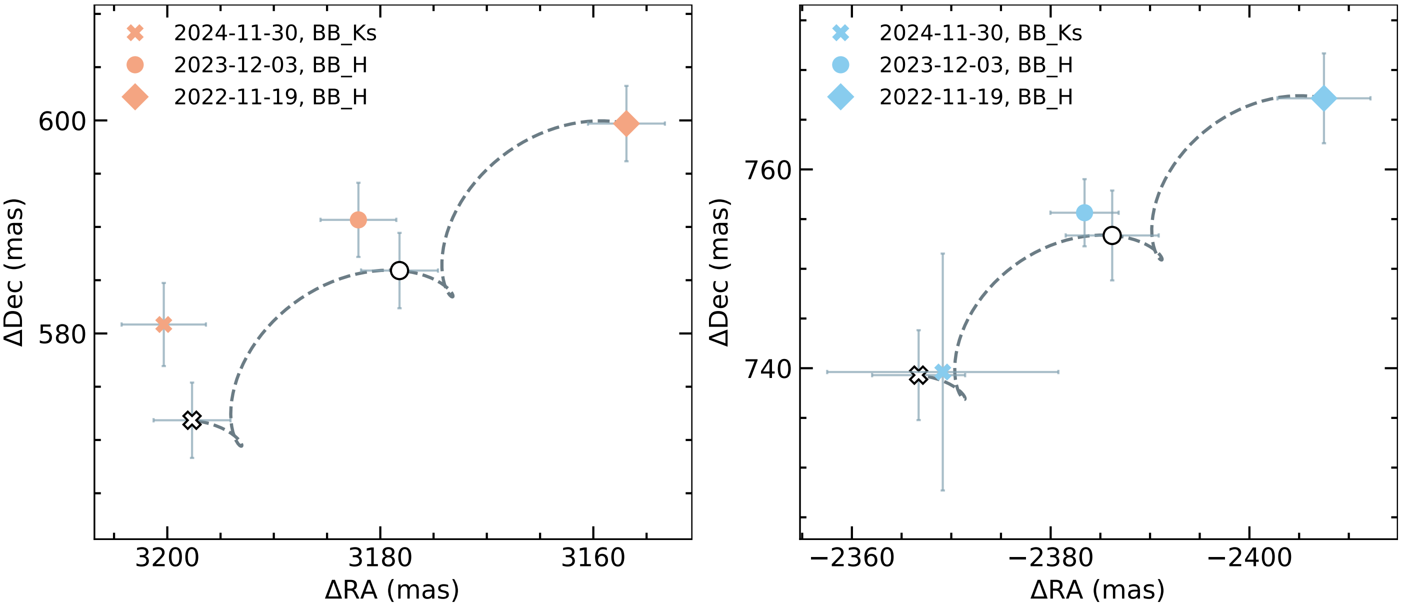

(a) Background object 1

(b) Background object 2

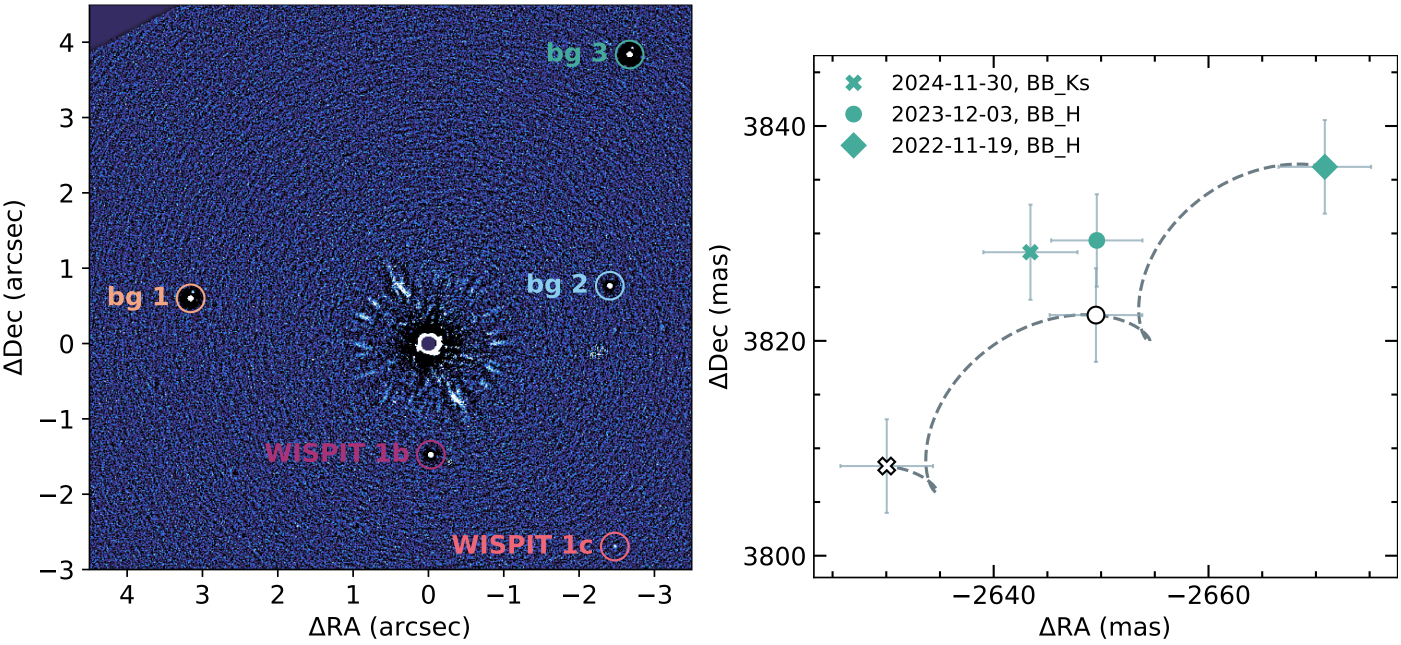

(c) Detection map

(d) Background object 3

Fig. F.1: Proper motion analysis of all background sources in the field of view. The detection map in panel (c) shows the positions of the sources relative to WISPIT 1 in the observation of epoch 2022-10-19 processed with unsharp masking. The three background sources are shown in panels (a), (b), and (d), respectively. Each epoch is marked with a unique marker shape; diamond (2022), circle (2023) and cross (2024). The coloured version of the marker indicates the measured position of the companion. The unfilled (black outline, white centre) version of this marker indicates the position that the companion would have been at at the corresponding date if it were a background object. The dashed curve depicts the parallactic track of a stationary background object from first epoch to last epoch. The χ^2 between the measured positions of background objects 1, 2 and 3 are 10.6, 1.1 and 32.2, respectively.

Appendix G: Median PSFs

All observations used to create the normalised median flux PSF in H-band and K_s-band are listed in Tables G.1 and G.2, respectively. Here 'Target name' denotes the commonly used designation for the source, and 'Archive name' corresponds to the name it is registered under in the ESO Science Archive Facility.

Table G.1: Flux observations used for constructing the median H-band PSF.

Target name	Archive name	Observation date
1RXS J114519.6-574925	2MASS J11452016-5749094	2018-05-14
1RXS J114542.7-573928	2MASS J11454278-5739285	2019-01-13
1RXS J114542.7-573928	2MASS J11454278-5739285	2023-04-20
1RXS J121010.3-485538	2MASS J12101065-4855476	2017-04-18
1RXS J123834.9-591645	2MASS J12383556-5916438	2019-01-03
1RXS J123834.9-591645	2MASS J12383556-5916438	2019-01-12
1RXS J123834.9-591645	2MASS J12383556-5916438	2023-07-14
1RXS J124830.1-594449	2MASS J12483152-5944493	2023-08-07
2MASS J12374883-5209463	2MASS J12374883-5209463	2018-12-30
2MASS J12374883-5209463	2MASS J12374883-5209463	2023-07-14
2MASS J13065439-4541313	2MASS J13065439-4541313	2018-04-08
2MASS J13065439-4541313	2MASS J13065439-4541313	2023-07-08
2MASS J13121764-5508258	2MASS J13121764-5508258	2018-05-15
2MASS J13334410-6359345	2MASS J13334410-6359345	2023-06-16
ASAS J114452-6438.9	2MASS J11445217-6438548	2018-05-14
ASAS J114452-6438.9	2MASS J11445217-6438548	2023-04-20
ASAS J122648-5214.8	2MASS J12264842-5215070	2018-12-30
ASAS J122648-5214.8	2MASS J12264842-5215070	2023-05-28
ASAS J124547-5411.0	2MASS J12454884-5410583	2018-04-30
ASAS J130550-5304.2	2MASS J13055087-5304181	2022-04-02
ASAS J131033-4816.9	2MASS J13103245-4817036	2018-05-01
CD-41 7947	2MASS J13343188-4209305	2023-08-07
CD-47 7559	2MASS J12220430-4841248	2017-04-18
CD-51 6900	2MASS J12404664-5211046	2018-04-30
CD-51 6900	2MASS J12404664-5211046	2023-05-30
CD-51 7268	2MASS J13064012-5159386	2018-04-30
CD-51 7268	2MASS J13064012-5159386	2023-06-15
CD-57 4328	2MASS J12113142-5816533	2018-12-22
CD-57 4328	2MASS J12113142-5816533	2019-02-18
CPD-50 5313	2MASS J12361767-5042421	2018-12-30
CPD-52 6110	2MASS J13015069-5304581	2019-01-08
CPD-56 5307	2MASS J12333381-5714066	2019-01-01
CPD-56 5307	2MASS J12333381-5714066	2019-01-14
CPD-56 5307	2MASS J12333381-5714066	2023-05-28
CPD-64 1859	2MASS J12192161-6454101	2023-06-17
PM J12160-5614	2MASS J12160114-5614068	2018-12-27
RX J1216.6-7007A	2MASS J12164023-7007361	2018-12-23
RX J1216.6-7007A	2MASS J12164023-7007361	2019-02-15
RX J1216.6-7007A	2MASS J12164023-7007361	2023-12-21
RX J1216.6-7007A	TYC 9231-1185-1	2024-06-10
RX J1220.0-5018A	2MASS J12195938-5018404	2018-12-30
RX J1220.0-5018A	2MASS J12195938-5018404	2023-06-17
RX J1230.5-5222	2MASS J12302957-5222269	2018-12-30
RX J1230.5-5222	2MASS J12302957-5222269	2022-03-30
UCAC2 12444765	2MASS J13095880-4527388	2018-05-01
UCAC4 186-087394	UCAC4 186-087394	2024-06-13
UNSW-V 514	2MASS J13174687-4456534	2018-05-28
V1257 Cen	2MASS J12505143-5156353	2019-01-12

Table G.2: Flux observations used for constructing the median K_s-band PSF.

Target name	Archive name	Observation date
1RXS J114542.7-573928	2MASS J11454278-5739285	2019-01-13
1RXS J123834.9-591645	2MASS J12383556-5916438	2019-01-03
1RXS J123834.9-591645	2MASS J12383556-5916438	2019-01-12
2MASS J12374883-5209463	2MASS J12374883-5209463	2018-12-30
2MASS J13065439-4541313	2MASS J13065439-4541313	2018-04-08
2MASS J13121764-5508258	2MASS J13121764-5508258	2018-05-15
ASAS J114452-6438.9	2MASS J11445217-6438548	2018-05-14
ASAS J122105-7116.9	2MASS J12210499-7116493	2019-01-12
ASAS J122648-5214.8	2MASS J12264842-5215070	2018-12-30
ASAS J124547-5411.0	2MASS J12454884-5410583	2018-04-30
ASAS J130550-5304.2	2MASS J13055087-5304181	2018-06-11
ASAS J130550-5304.2	2MASS J13055087-5304181	2018-07-05
ASAS J131033-4816.9	2MASS J13103245-4817036	2018-05-01
CD-49 7280	2MASS J12405458-5031550	2018-12-30
CD-51 6900	2MASS J12404664-5211046	2018-04-30
CD-57 4328	2MASS J12113142-5816533	2018-12-22
CD-57 4328	2MASS J12113142-5816533	2019-02-18
CPD-49 4947	2MASS J12121119-4950081	2018-12-22
CPD-50 5313	2MASS J12361767-5042421	2018-12-30
CPD-53 5235	2MASS J12365895-5412178	2019-01-01
CPD-53 5235	2MASS J12365895-5412178	2019-01-13
CPD-56 5307	2MASS J12333381-5714066	2019-01-01
CPD-56 5307	2MASS J12333381-5714066	2019-01-14
PM J12160-5614	2MASS J12160114-5614068	2018-12-27
RX J1216.6-7007A	2MASS J12164023-7007361	2018-12-23
RX J1216.6-7007A	2MASS J12164023-7007361	2019-02-15
RX J1220.0-5018A	2MASS J12195938-5018404	2018-12-30
RX J1230.5-5222	2MASS J12302957-5222269	2018-12-30
UCAC2 12444765	2MASS J13095880-4527388	2018-05-01
UCAC4 186-087394	2MASS J12510556-5253121	2019-01-08
UNSW-V 514	2MASS J13174687-4456534	2018-05-28
V1257 Cen	2MASS J12505143-5156353	2019-01-12